

# Rheo-SINDy: Finding a constitutive model from rheological data for complex fluids using sparse identification for nonlinear dynamics

Takeshi Sato,<sup>1, a)</sup> Souta Miyamoto,<sup>2</sup> and Shota Kato<sup>3</sup>

<sup>1)</sup>*Advanced Manufacturing Technology Institute, Kanazawa University, Kanazawa 920-1192, Japan*

<sup>2)</sup>*Department of Chemical Engineering, Graduate School of Engineering, Kyoto University, Kyoto 615-8510, Japan*

<sup>3)</sup>*Graduate School of Informatics, Kyoto University, Kyoto 606-8501, Japan*

(Dated: 7 May 2024)

Rheology plays a pivotal role in understanding the flow behavior of fluids by discovering governing equations that relate deformation and stress, known as constitutive equations. Despite the importance of these equations, current methods for deriving them lack a systematic methodology, often relying on expert knowledge and incurring substantial costs. To overcome this problem, we propose a novel method named *Rheo-SINDy*, which employs the sparse identification of nonlinear dynamics (SINDy) algorithm for discovering constitutive models from rheological data. *Rheo-SINDy* was applied to five distinct scenarios, four with well-established constitutive equations and one without predefined equations. Our results demonstrate that *Rheo-SINDy* successfully identified accurate models for the known constitutive equations and derived physically plausible approximate models for the scenario without established equations. Notably, the identified approximate models can accurately reproduce nonlinear shear rheological properties, including shear thinning. These findings validate the robustness of *Rheo-SINDy* in handling real-world data complexities and underscore its efficacy as a tool for advancing the development of data-driven approaches in rheology.

## I. INTRODUCTION

Mathematical models grounded in physical laws offer profound insights into the behavior of complex systems across science and engineering. These models clarify the underlying mechanisms governing system dynamics and empower predictions and innovations in technology and natural science. Traditionally, model derivation has leaned heavily on theoretical and empirical knowledge, often requiring expert knowledge and intuition. Data-driven methods have become capable of assisting in developing mathematical models and constructing models that provide advanced predictions<sup>1</sup>. These data-driven methods involve the sparse identification<sup>2–5</sup>, symbolic regression<sup>6–11</sup>, and physics-informed machine learning methods<sup>12–15</sup>. These methods have emerged as powerful tools for deriving governing equations directly from data, overcoming the limitations of conventional expert-dependent approaches.

*Rheology* is one of the scientific fields that address the properties of flowing matter, which plays a crucial role in many industries, such as designs of chemical processes, by providing insights into the flow behavior of complex fluids. One of the roles of rheology is to discover or derive governing equations that relate deformation and stress, referred to as *constitutive equations*<sup>16</sup>. Accurate constitutive equations are necessary to predict the flows of complex fluids under complex boundary conditions. Derivations of constitutive equations starting from the principles of continuum mechanics have achieved significant success in the field of rheology, yielding several practical constitutive equations<sup>16</sup>. Nevertheless, it is generally difficult to theoretically obtain constitutive equations for complex fluids from molecular models. Such cases usually

explore mesoscopic coarse-grained models, which are based on molecular theories and suitable for numerical simulations. For example, for polymeric liquids, standard molecular theories have been proposed<sup>17,18</sup> and refined mesoscopic models have been constructed based on them<sup>19–21</sup>. In these models, the motion of individual (coarse-grained) molecules is numerically tracked. Although these models can reproduce rheological data with high accuracy, they require significantly more computational time compared to constitutive equations. Thus, a clear methodology is desired for obtaining constitutive equations from available *data*.

Data-driven methods have addressed the aforementioned challenges and advanced rheological studies such as constitutive modeling, flow predictions of complex fluids, and model selection<sup>22,23</sup>. Some applications have successfully identified constitutive relations of complex fluids or governing equations to predict the dynamics of fluids with knowledge of rheology. These studies have employed neural networks (NNs), including deep NN<sup>24</sup>, graph NN<sup>25</sup>, recurrent NN<sup>26</sup>, physics-informed NN<sup>27–29</sup>, multi-fidelity NN<sup>30</sup>, and tensor basis NN<sup>31</sup>. Gaussian process regressions (GPRs) have also been employed, for example, for strain-rate dependent viscosity<sup>32</sup> or for viscoelastic properties<sup>33–36</sup>.

Despite the success of NNs and GPRs, their black-box nature often obscures the underlying physics, making symbolic regression techniques more appealing for transparency and interoperability<sup>1</sup>. For example, this technique can successfully identify the governing equations for fluid flows<sup>8</sup>. Moreover, the sparse identification of nonlinear dynamics (SINDy)<sup>2</sup>, which is one of such methods, has been utilized to track (reduced order) dynamics in the field of fluid mechanics<sup>37</sup>. Inspired by these successes, symbolic regression methods have recently started to be used in the field of rheology as well. For example, Mohammadamin and coworkers relied on SINDy for flexibly identifying the constitutive equations for

<sup>a)</sup>Electronic mail: takeshis@se.kanazawa-u.ac.jp

an elasto-visco-plastic fluid<sup>38</sup>. Generally, the performance of SINDy is significantly influenced by the training data collection method, the candidate terms selected, and the optimization method. However, a comprehensive study to test SINDy for rheological data has not yet been conducted. Before applying SINDy to real-world rheological data, it is highly desirable to investigate fundamental learning strategies such as how to collect training data among various rheological tests and which optimization method to implement.

In this study, we employ SINDy to find constitutive models from rheological data, which we call as *Rheo-SINDy*. For the *Rheo-SINDy* regressions, we prepare a training dataset including stress trajectories under simple and oscillatory shear flows and choose the candidate terms based on rheological knowledge of fundamental constitutive equations. Furthermore, multiple optimization methods are compared to find the effective ones for obtaining constitutive equations. This paper demonstrates five case studies. The first four cases verify the performance of *Rheo-SINDy* to identify the known constitutive equations, while the last one attempts to find the unknown constitutive equation for a coarse-grained mesoscopic model. Through the case studies, we validate the effectiveness of *Rheo-SINDy* and propose a strategy to find constitutive equations from rheological data. The details are shown below.

## II. METHODS

We use a data-driven method known as a sparse identification of nonlinear dynamics (SINDy), which was originally developed by Brunton and coworkers<sup>2</sup>, to obtain constitutive equations of complex fluid dynamics. The SINDy framework considers dynamical systems generally expressed by the following differential equation:

$$\frac{d\mathbf{x}(t)}{dt} = \dot{\mathbf{x}}(t) = \mathbf{f}[\mathbf{x}(t)], \quad (1)$$

where the vector  $\mathbf{x}(t)$  represents the state of a system at time  $t$  and the function  $\mathbf{f}[\mathbf{x}(t)]$  determines the dynamics of the state  $\mathbf{x}(t)$ . The basic idea of SINDy is to find dominant terms for describing the dynamics out of numerous candidates using a sparse identification method. One can determine the (sparse) representation of  $\mathbf{f}$  by a dataset including a collection of  $\mathbf{x}(t)$  and  $\dot{\mathbf{x}}(t)$ . The regression to points of  $\mathbf{x}(t)$  and  $\dot{\mathbf{x}}(t)$  is computed with sparsity-promoting techniques, such as  $\ell_1$ -regularization.

In the rheological community, it is of great importance to determine a relation between stress and strain rate. This relation is a so-called constitutive model or constitutive equation. Most constitutive equations are differential equations that depend on the (extra) stress tensor  $\boldsymbol{\tau}$  and velocity gradient tensor  $\boldsymbol{\kappa}$ . We prefer to use the so-called extra stress tensor  $\boldsymbol{\tau}$  as the stress tensor because this tensor satisfies  $\boldsymbol{\tau} = \mathbf{0}$  at equilibrium<sup>16</sup>, which is convenient for the SINDy regression. The total stress tensor  $\boldsymbol{\sigma}$  can be obtained by the relation  $\boldsymbol{\sigma} = \boldsymbol{\tau} + G\mathbf{I}$ , where  $G$  is the modulus and  $\mathbf{I}$  is the unit tensor. A general

form for such constitutive equations can be written as

$$\frac{d\boldsymbol{\tau}(t)}{dt} = \dot{\boldsymbol{\tau}}(t) = \mathbf{f}[\boldsymbol{\tau}(t), \boldsymbol{\kappa}(t)]. \quad (2)$$

The velocity gradient tensor  $\boldsymbol{\kappa}(t)$  is manipulated during rheological measurements. In formal constitutive equations, the time derivative should be frame-invariant, such as the upper-convected derivative<sup>16</sup>. As shown later in Sec. IV, the terms that appeared in the upper-convected derivative are recovered by the SINDy regressions.

We use the SINDy algorithm to find constitutive equations for complex fluids from data, and we refer to this technique as *Rheo-SINDy*. *Rheo-SINDy* requires three types of training data, two of which are transient stress data  $\mathbf{T}$  and those time derivatives  $\dot{\mathbf{T}}$  summarized as the following matrices:

$$\mathbf{T} = \begin{bmatrix} \tau_{xx} & \tau_{yy} & \cdots & \tau_{zx} \end{bmatrix} = \begin{bmatrix} \tau_{xx}(t_1) & \tau_{yy}(t_1) & \cdots & \tau_{zx}(t_1) \\ \tau_{xx}(t_2) & \tau_{yy}(t_2) & \cdots & \tau_{zx}(t_2) \\ \vdots & \vdots & \ddots & \vdots \\ \tau_{xx}(t_n) & \tau_{yy}(t_n) & \cdots & \tau_{zx}(t_n) \end{bmatrix} \quad (3)$$

and

$$\dot{\mathbf{T}} = \begin{bmatrix} \dot{\tau}_{xx} & \dot{\tau}_{yy} & \cdots & \dot{\tau}_{zx} \end{bmatrix} = \begin{bmatrix} \dot{\tau}_{xx}(t_1) & \dot{\tau}_{yy}(t_1) & \cdots & \dot{\tau}_{zx}(t_1) \\ \dot{\tau}_{xx}(t_2) & \dot{\tau}_{yy}(t_2) & \cdots & \dot{\tau}_{zx}(t_2) \\ \vdots & \vdots & \ddots & \vdots \\ \dot{\tau}_{xx}(t_n) & \dot{\tau}_{yy}(t_n) & \cdots & \dot{\tau}_{zx}(t_n) \end{bmatrix}, \quad (4)$$

where  $\mathbf{t}_{\mu\nu}$  ( $\mu, \nu \in \{xx, yy, zz, xy, yz, zx\}$ ) is the stress data for  $n$  sequential times. In this study, the stress data are collected by applying  $\boldsymbol{\kappa}(t)$  to systems of prescribed constitutive equations or mesoscopic models of viscoelastic fluids. The time derivatives of the stress data  $\dot{\mathbf{T}}$  are computed by a numerical differentiation method. The remaining required data is the velocity gradient data  $\mathbf{K}$  summarized as

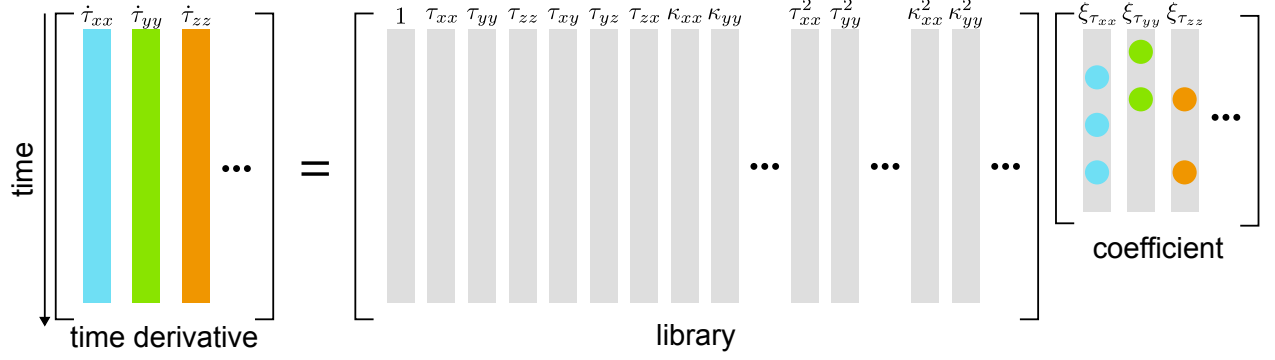
$$\mathbf{K} = \begin{bmatrix} k_{xx} & k_{yy} & \cdots & k_{zx} \end{bmatrix} = \begin{bmatrix} \kappa_{xx}(t_1) & \kappa_{yy}(t_1) & \cdots & \kappa_{zx}(t_1) \\ \kappa_{xx}(t_2) & \kappa_{yy}(t_2) & \cdots & \kappa_{zx}(t_2) \\ \vdots & \vdots & \ddots & \vdots \\ \kappa_{xx}(t_n) & \kappa_{yy}(t_n) & \cdots & \kappa_{zx}(t_n) \end{bmatrix}, \quad (5)$$

where  $\mathbf{k}_{\mu\nu}$  ( $\mu, \nu \in \{x, y, z\}$ ) is the velocity gradient data for  $n$  time steps.

In *Rheo-SINDy*, we construct a library matrix of functions  $\boldsymbol{\Theta}$ , which includes various nonlinear functions, expressed as

$$\boldsymbol{\Theta} = [\mathbf{1} \quad \mathbf{T} \quad \mathbf{K} \quad (\mathbf{T} \otimes \mathbf{T}) \quad (\mathbf{T} \otimes \mathbf{K}) \quad (\mathbf{K} \otimes \mathbf{K}) \quad \cdots], \quad (6)$$

where  $\mathbf{T} \otimes \mathbf{K}$ , for example, denotes all possible combinations of the products of the row components in  $\mathbf{T}$  and  $\mathbf{K}$  for each time  $t_i$  ( $1 \leq i \leq n$ ). The library  $\boldsymbol{\Theta}$  can incorporate not only polynomials but also other functions, such as sinusoidal functions. If the library contains unnecessary functions or does not contain necessary functions, the correct expression cannot be obtained by *Rheo-SINDy*. Thus, functions to be included in the library must be selected carefully by utilizing expertise in rheology and knowledge of the target data. The detailed procedure varies from case to case and is provided in Sec. IV.

FIG. 1. Schematic illustration of *Rheo-SINDy*.

Using these expressions, we can rewrite Eq. (2) as

$$\dot{T} = \Theta \Xi, \quad (7)$$

where  $\Xi$  is the sparse coefficient matrix written as

$$\Xi = [\xi_{xx} \ \xi_{yy} \ \dots \ \xi_{zx}] = \begin{bmatrix} \xi_{xx,1} & \xi_{yy,1} & \dots & \xi_{zx,1} \\ \xi_{xx,2} & \xi_{yy,2} & \dots & \xi_{zx,2} \\ \vdots & \vdots & \ddots & \vdots \\ \xi_{xx,N_\Theta} & \xi_{yy,N_\Theta} & \dots & \xi_{zx,N_\Theta} \end{bmatrix}, \quad (8)$$

where  $N_\Theta$  is the total number of library functions. To determine the coefficients  $\Xi$ , we solve the following optimization problem for each row:

$$\hat{\xi}_{\mu\nu} = \underset{\xi_{\mu\nu}}{\operatorname{argmin}} \|\dot{t}_{\mu\nu} - \Theta \xi_{\mu\nu}\|_2^2 + R(\xi_{\mu\nu}), \quad (9)$$

where  $\hat{\xi}_{\mu\nu}$  is the optimized sparse vector,  $\|\dots\|_2$  is the  $\ell_2$ -norm defined as

$$\|x\|_2 = \left( \sum_i x_i^2 \right)^{1/2}, \quad (10)$$

and  $R(\xi_{\mu\nu})$  is the regularization term. To obtain a sparse solution of  $\Xi$  from rheological data, we apply the following five methods<sup>37</sup>: (i) the sequentially thresholded least square algorithm (STLSQ), (ii) sequentially thresholded Ridge regression (STRidge), (iii) least absolute shrinkage and selection operator (Lasso), (iv) Elastic-Net (E-Net), and (v) adaptive-Lasso (a-Lasso). These methods employ different regularization terms to obtain sparse solutions (see Sec. S1 in the supplementary material for details). Each method has a hyperparameter  $\alpha$  to penalize the solution complexity, which is to be tuned for obtaining good predictive yet parsimonious representations. For this purpose, we test various  $\alpha$  values and pick the one with the smallest number of terms among the results whose error has the same order as the minimum error (when  $\alpha$  is sufficiently small).

In this study, we focus on *shear* rheological measurements that give fundamental rheological properties because they are well-studied and suitable for discussing the applicability of our method to rheology data. Under shear flow, among the

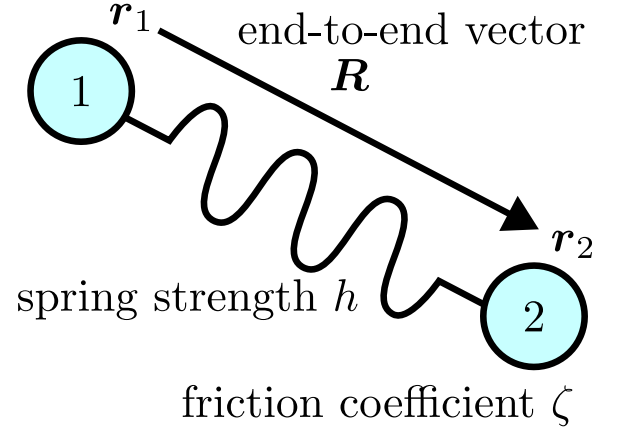


FIG. 2. Schematic illustration of the dumbbell model.

components of  $\kappa$ , only  $\kappa_{xy}$  has non-zero values. Here,  $x$  is the velocity direction, and  $y$  is the velocity gradient direction. Since the major stress components are  $\tau_{xx}$ ,  $\tau_{yy}$ ,  $\tau_{zz}$ , and  $\tau_{xy}$  under shear flow, we only use these components to conduct *Rheo-SINDy*.

### III. CASE STUDIES

For case studies, we first test whether *Rheo-SINDy* can find appropriate constitutive equations from training data generated by phenomenological constitutive equations, namely the Upper Convected Maxwell (UCM) model and the Giesekus model (the details are summarized in Sec. S2 in the supplementary material). Subsequently, we apply *Rheo-SINDy* to data generated by several dumbbell-based models. This section provides a brief overview of the dumbbell models used in this study and the conditions for creating the training datasets.

The dumbbell-based models have been widely utilized in numerous previous studies for the computation of viscoelastic fluids and are regarded as the standard mesoscopic model for viscoelastic fluids<sup>39</sup>. As illustrated in Fig. 2, a dumbbell consists of two beads (indexed as 1 or 2) and a spring that connects them. The Langevin equations for the positions of

the two beads  $\mathbf{r}_{1/2}(t)$  can be written as

$$\zeta \left[ \frac{d\mathbf{r}_i(t)}{dt} - \boldsymbol{\kappa} \cdot \mathbf{r}_i(t) \right] = -h(t) \{ \mathbf{r}_i(t) - \mathbf{r}_j(t) \} + \mathbf{F}_{Bi}(t), \quad (11)$$

with  $(i, j) = (1, 2)$  or  $(2, 1)$ . Here,  $\zeta$  is the friction coefficient,  $h(t)$  is the spring strength, and  $\mathbf{F}_{Bi}(t)$  is the Brownian force acting on the bead  $i$ . The time evolution equation for the end-to-end vector  $\mathbf{R}(t) (= \mathbf{r}_2(t) - \mathbf{r}_1(t))$  of the beads is thus obtained as

$$\zeta \left[ \frac{d\mathbf{R}(t)}{dt} - \boldsymbol{\kappa} \cdot \mathbf{R}(t) \right] = -2h(t)\mathbf{R}(t) + \{ \mathbf{F}_{B2}(t) - \mathbf{F}_{B1}(t) \}. \quad (12)$$

The Brownian force is characterized by the first and second-moment averages as

$$\langle \mathbf{F}_{Bi}(t) \rangle = \mathbf{0} \quad (13)$$

and

$$\langle \mathbf{F}_{Bi}(t) \mathbf{F}_{Bj}(t') \rangle = 2\zeta k_B T \delta_{ij} \delta(t - t') \mathbf{I}, \quad (14)$$

where  $k_B$  is the Boltzmann constant and  $T$  is the temperature. From the end-to-end vector  $\mathbf{R}(t)$ , the stress tensor can be expressed as

$$\boldsymbol{\tau}(t) = \rho \langle h(t) \mathbf{R}(t) \mathbf{R}(t) \rangle - \rho k_B T \mathbf{I}, \quad (15)$$

where  $\rho$  is the density of dumbbells.

There are several expressions for the spring strength  $h(t)$ . The most basic one is the Hookean spring, defined as

$$h(t) = h_{\text{eq}} = \frac{3k_B T}{n_K b_K^2}, \quad (16)$$

where  $n_K$  is the number of Kuhn segments per spring and  $b_K$  is the Kuhn length. Reproduction of some nonlinear rheological properties, such as shear thinning under shear flow, necessitates dealing with finite extensible nonlinear elastic (FENE) effects. Although the exact expression for FENE springs is given by the inverse Langevin function, the following empirical expression is widely used<sup>39</sup>:

$$h(t) = h_{\text{eq}} \frac{1 - \langle R_{\text{eq}}^2 \rangle / R_{\text{max}}^2}{1 - \langle \mathbf{R}^2(t) \rangle / R_{\text{max}}^2}, \quad (17)$$

where  $\langle R_{\text{eq}}^2 \rangle^{1/2} = (n_K)^{1/2} b_K$  is the equilibrium length of the springs, and  $R_{\text{max}} = n_K b_K$  is the maximum length of the springs. As shown later in Sec. III C, a constitutive equation cannot be analytically obtained for the FENE dumbbell model. To address the FENE spring more analytically, the following approximate expression of the FENE spring has been proposed<sup>39</sup>:

$$h(t) = h_{\text{eq}} \frac{1 - \langle R_{\text{eq}}^2 \rangle / R_{\text{max}}^2}{1 - \langle \mathbf{R}^2(t) \rangle / R_{\text{max}}^2} = h_{\text{eq}} f_{\text{FENE}}(t). \quad (18)$$

This spring is referred to as the FENE-P spring. Here, “P” means Peterlin, who proposed the approximate form of the

FENE spring law. The average appearing in Eq. (18) makes it possible to obtain the analytical constitutive equation.

We use  $\lambda = \zeta / 4h_{\text{eq}}$  as the unit time and  $G = \rho k_B T$  as the unit stress for the dumbbell models. To simplify the expressions, we omit the tilde representing dimensionless quantities in what follows.

### A. Hookean Dumbbell Model

The most basic dumbbell model is the Hookean dumbbell model, where Hookean springs are employed (cf. Eq. (16)). From Eqs. (12), (15), and (16), the Hookean dumbbell model reduces to the constitutive equation for the UCM model (cf. Eq. (S5) in the supplementary material) in the limit of  $N_p \rightarrow \infty$  with  $N_p$  being the number of dumbbells. Specifically, the constitutive equations of the UCM model for each stress component under shear flow are expressed as

$$\dot{\tau}_{xx} = -\tau_{xx} + 2\tau_{xy}\kappa_{xy}, \quad (19)$$

$$\dot{\tau}_{yy/zz} = \tau_{yy/zz} = 0, \quad (20)$$

$$\dot{\tau}_{xy} = -\tau_{xy} + \kappa_{xy} + \tau_{yy}\kappa_{xy} = -\tau_{xy} + \kappa_{xy}. \quad (21)$$

Here, “yy/zz” in Eq. (20) means “yy or zz”.

For the Hookean dumbbell model, we generate training data by Brownian dynamics (BD) simulations with the finite numbers of dumbbells ( $N_p \in \{10^3, 10^4, 10^5\}$ ). We apply the oscillatory shear flow,  $\gamma(t) = \gamma_0 \sin(\omega t)$  (i.e.,  $\kappa_{xy}(t) = \dot{\gamma}(t) = \gamma_0 \omega \cos(\omega t)$ ), with  $\gamma_0 = 2$  and  $\omega = 0.5$ , over a period from  $t = 0$  to  $t = 100$ . The simulations are run with  $\Delta t = 1 \times 10^{-3}$  for  $0 \leq t \leq 100$  and data are collected at the interval of  $\Delta t_{\text{train}} = 1 \times 10^{-2}$ . Each simulation is conducted with five different random seeds, and their average data is used for training. Due to the characteristics of the BD simulation, the training data inherently include noise originating from the finite  $N_p$ . We here test whether *Rheo-SINDy* can find from the noisy data the constitutive equations for the UCM model shown in Eq. (19)–(21).

### B. FENE-P Dumbbell Model

We next address the so-called FENE-P dumbbell model, where Eq. (18) is utilized as the spring strength. As shown below, the FENE-P dumbbell model has an analytical solution and is utilized for various flow problems<sup>40,41</sup>.

Due to the assumption shown in Eq. (18), a simple representation of the time evolution for the conformation tensor  $\mathbf{C} = \langle \mathbf{R}(t) \mathbf{R}(t) \rangle$  can be obtained as

$$\frac{d\mathbf{C}}{dt} - \mathbf{C} \cdot \boldsymbol{\kappa}^+ - \boldsymbol{\kappa} \cdot \mathbf{C} = -f_{\text{FENE}}(t)\mathbf{C} + \frac{n_K}{3}\mathbf{I}, \quad (22)$$

where  $\boldsymbol{\kappa}^+$  is the transposed  $\boldsymbol{\kappa}$ . The stress tensor is thus obtained by

$$\boldsymbol{\tau}(t) = \rho h(t) \mathbf{C}(t) - \rho k_B T \mathbf{I}. \quad (23)$$



Under shear flow, Eq. (22) reduces to the following expressions:

$$\dot{C}_{xx} = -f_{\text{FENE}}C_{xx} + 2C_{xy}\kappa_{xy} + \frac{n_K}{3}, \quad (24)$$

$$\dot{C}_{yy/zz} = -f_{\text{FENE}}C_{yy/zz} + \frac{n_K}{3}, \quad (25)$$

$$\dot{C}_{xy} = -f_{\text{FENE}}C_{xy} + C_{yy}\kappa_{xy}. \quad (26)$$

Using *Rheo-SINDy*, we test whether or not Eqs. (24)–(26) can be discovered from the data.

Although it has not been as widely recognized due to its complexity, the FENE-P dumbbell model can also be expressed in the form of the constitutive equation (i.e., the stress expression)<sup>42</sup>. From the textbook of Bird and coworkers<sup>39</sup>, the constitutive equation for the FENE-P model is

$$\frac{d\boldsymbol{\tau}}{dt} - \boldsymbol{\tau} \cdot \boldsymbol{\kappa}^+ - \boldsymbol{\kappa} \cdot \boldsymbol{\tau} = -f_{\text{FENE}}(t)\boldsymbol{\tau} + 2\mathbf{D} + \frac{D \ln Z}{Dt}(\boldsymbol{\tau} + \mathbf{I}), \quad (27)$$

where  $D(\cdots)/Dt$  is the substantial derivative and  $Z$  is the function expressed as

$$Z = \frac{1}{1 - \langle R^2(t)/R_{\text{max}}^2 \rangle} = 1 + \frac{1}{3n_K Z_{\text{eq}}^{-1}}(\text{tr}\boldsymbol{\tau} + 3). \quad (28)$$

Here,  $Z_{\text{eq}}$  indicates  $Z$  at equilibrium. From Eq. (28), we can see that  $\text{tr}\boldsymbol{\tau}$  is tightly related to the (squared) length of dumbbells. Since we do not address the spatial gradient in rheological calculations,  $D(\cdots)/Dt$  simply reduces to  $d(\cdots)/dt$ . Using Eqs. (22), (27), and (28), the constitutive equations for the FENE-P dumbbell model under shear flow can be expressed as

$$\begin{aligned} \dot{\tau}_{xx} = & -\left\{1 + \frac{1}{3(n_K - 1)}\right\} \tau_{xx} - \frac{1}{3(n_K - 1)}(\tau_{yy} + \tau_{zz}) \\ & - \frac{1}{9n_K(n_K - 1)}(\text{tr}\boldsymbol{\tau})^2 - \frac{1}{3n_K}\left(2 + \frac{1}{n_K - 1}\right)\text{tr}\boldsymbol{\tau}\tau_{xx} \\ & + 2\left\{1 + \frac{1}{3(n_K - 1)}\right\} \tau_{xy}\kappa_{xy} - \frac{1}{9n_K(n_K - 1)}(\text{tr}\boldsymbol{\tau})^2\tau_{xx} \\ & + \frac{2}{3(n_K - 1)}\tau_{xx}\tau_{xy}\kappa_{xy}, \end{aligned} \quad (29)$$

$$\begin{aligned} \dot{\tau}_{yy/zz} = & -\left\{1 + \frac{1}{3(n_K - 1)}\right\} \tau_{yy/zz} - \frac{1}{3(n_K - 1)}(\tau_{xx} + \tau_{zz/yy}) \\ & - \frac{1}{9n_K(n_K - 1)}(\text{tr}\boldsymbol{\tau})^2 - \frac{1}{3n_K}\left(2 + \frac{1}{n_K - 1}\right)\text{tr}\boldsymbol{\tau}\tau_{yy/zz} \\ & + \frac{2}{3(n_K - 1)}\tau_{xy}\kappa_{xy} - \frac{1}{9n_K(n_K - 1)}(\text{tr}\boldsymbol{\tau})^2\tau_{yy/zz} \\ & + \frac{2}{3(n_K - 1)}\tau_{yy/zz}\tau_{xy}\kappa_{xy}, \end{aligned} \quad (30)$$

$$\begin{aligned} \dot{\tau}_{xy} = & -\tau_{xy} + \kappa_{xy} + \tau_{yy}\kappa_{xy} - \frac{1}{3n_K}\left(2 + \frac{1}{n_K - 1}\right)\text{tr}\boldsymbol{\tau}\tau_{xy} \\ & - \frac{1}{9n_K(n_K - 1)}(\text{tr}\boldsymbol{\tau})^2\tau_{xy} + \frac{2}{3(n_K - 1)}\tau_{xy}^2\kappa_{xy}. \end{aligned} \quad (31)$$

For the derivation, please refer to Sec. S5 in the supplementary material. From Eqs. (29)–(31), the constitutive equation for the FENE-P model can be expressed by a polynomial of up to a third degree in  $\boldsymbol{\tau}$  and  $\boldsymbol{\kappa}$ . Here, we note that Eqs. (29)–(31) become equivalent to the UCM model shown in Eqs. (19)–(21) in the limit of  $n_K \rightarrow \infty$ .

To generate noise-free training data, we solve Eqs. (23)–(26) with  $n_K = 10$  and  $\Delta t = 1 \times 10^{-4}$  for  $0 \leq t \leq 100$ . We apply the oscillatory shear flow with  $\gamma_0 = 2$  and various  $\omega$  values ( $\omega \in \{0.1, 0.2, \dots, 1\}$ ). From the computed stress data, we collect data at the interval of  $\Delta t_{\text{train}} = 1 \times 10^{-2}$ .

### C. FENE Dumbbell Model

We finally address the FENE dumbbell model, where the spring strength is represented by Eq. (17). Since the FENE dumbbell model does not use any simplification for the spring strength (e.g., Peterlin approximation shown in Eq. (18)), its analytical constitutive equation has not been obtained. We apply *Rheo-SINDy* to this case to see if an *approximate* constitutive equation can be obtained. The obtained equations are validated by comparing the data obtained by numerically solving them with the data obtained by BD simulations.

The training data are generated by the BD simulations using Eqs. (12)–(15) and (17) with  $n_K = 10$ ,  $N_p = 10^4$ , and  $\Delta t = 1 \times 10^{-4}$  for  $0 \leq t \leq 100$ . We apply the oscillatory shear flows with the same parameters as those in the FENE-P dumbbell model. The BD simulation results with five different random seeds are averaged for each condition. Since we do not use any approximation for the spring strength, the values of  $h(t)$  differ for each individual dumbbell. From the computed stress data, we collected data at the interval of  $\Delta t_{\text{train}} = 1 \times 10^{-2}$ .

## IV. RESULTS AND DISCUSSIONS

In this section, we present the results of the case studies for the dumbbell models. From the case studies on phenomenological constitutive equations shown in Sec. S3 in the supplementary material, we have made the following two findings: (i) taking shear rheological data by an oscillatory shear test is more appropriate than by a simple (constant) shear test, and (ii) among the five optimization methods shown in Sec. II, the STRidge or a-Lasso is superior to the other three methods. Thus, in what follows, we generate the training data using the oscillatory shear test and employ the STRidge and a-Lasso as optimization methods. To discuss the effect of the hyperparameter  $\alpha$ , we also examine the results with  $\alpha$ , not selected in the proposed method.

### A. Hookean Dumbbell Model

We first explain the results for the Hookean dumbbell model. We here used the polynomial library that includes up to second order terms of  $\tau_{xx}$ ,  $\tau_{yy}$ ,  $\tau_{xy}$ , and  $\kappa_{xy}$ . Thus, the total number of candidate terms was  $N_{\Theta} = 15$  for each component.

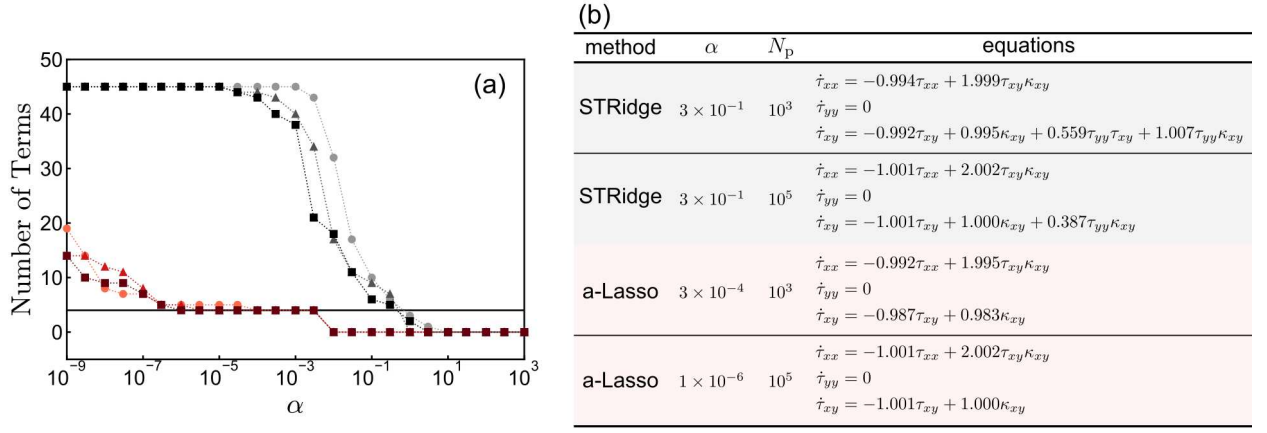


FIG. 3. (a) The total number of terms and (b) the constitutive equations obtained by *Rheo-SINDy* with the STRidge (black) and a-Lasso (red) for the Hookean dumbbell model (Eqs. (19)–(21)). In (a), the horizontal line indicates the correct number of terms, and circle, triangle, and square symbols represent the results for  $N_p = 10^3$ ,  $10^4$ , and  $10^5$ , respectively.

Figure 3 shows the *Rheo-SINDy* results for the Hookean dumbbell model with the different numbers of dumbbells. We note that the standard deviation of  $\tau$  in the training data decreases proportionally with  $N_p^{-1/2}$ . From Fig. 3(a), as the value of  $N_p$  increases, sparser solutions are obtained, especially for *Rheo-SINDy* with the STRidge. Unlike the case of the UCM model (cf. Fig. S1 in the supplementary material), which can be considered as the “noise-free” case of the Hookean dumbbell model, the STRidge provides the correct number of terms only within a narrow range of  $\alpha$  values. Nevertheless, if we choose the appropriate  $\alpha$  value, the (nearly) correct constitutive equations can be found by the STRidge, as shown in the upper part of Fig. 3(b). We note that the terms containing  $\tau_{yy}$  appear in the time evolution equation for  $\tau_{xy}$  obtained by the STRidge. Although these terms do not affect the predictions because  $\tau_{yy} = 0$ , these terms do not appear in the correct equation. We speculate that the appearance of these terms is due to the correlation effects of the noise in  $R_x$  and  $R_y$  on the stress (cf. Eq. (15)). When comparing the STRidge and a-Lasso, it is evident that the a-Lasso provides stable and sparse solutions across a broader range of  $\alpha$  values, regardless of the  $N_p$  value. Furthermore, we confirm that the correct equations can be obtained using the a-Lasso, as shown in the lower part of Fig. 3(b). This partially suggests the effectiveness of the a-Lasso in discovering essential terms from noisy data.

### B. FENE-P Dumbbell Model

We next examine whether *Rheo-SINDy* can find more complex differential equations (i.e., the FENE-P dumbbell model) than the UCM model and the Giesekus model. We utilized *Rheo-SINDy* with  $T$  replaced by  $C$  to discover the differential equations for the conformation tensor  $C$  of the FENE-P dumbbell model explained in Sec. III B. In this case, we pre-

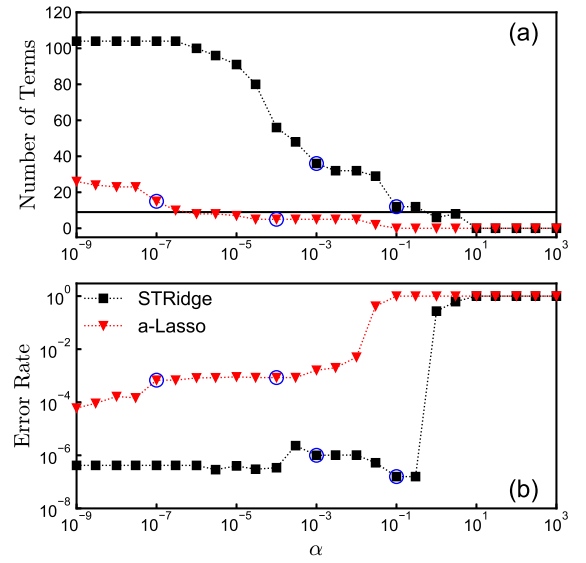


FIG. 4. (a) The total number of terms and (b) the error rate of the constitutive equations obtained by *Rheo-SINDy* with the STRidge (black squares) and a-Lasso (red reverse triangles) for the FENE-P dumbbell model in conformation expression (Eqs. (24)–(26) with  $n_K = 10$ ). The horizontal line in (a) indicates the correct number of terms. The blue circles represent the  $\alpha$  values selected for test simulations.

pared the following custom library:

$$\Theta = \begin{bmatrix} 1 & \Omega(t_1) & \Omega^2(t_1) & f_{\text{FENE}}(t_1)\Omega(t_1) \\ 1 & \Omega(t_2) & \Omega^2(t_2) & f_{\text{FENE}}(t_2)\Omega(t_2) \\ \vdots & \vdots & \vdots & \vdots \\ 1 & \Omega(t_n) & \Omega^2(t_n) & f_{\text{FENE}}(t_n)\Omega(t_n) \end{bmatrix}, \quad (32)$$

where  $\Omega$  consists of non-zero components of  $C$  under shear flow ( $C_{xx}$ ,  $C_{yy}$ ,  $C_{zz}$ , and  $C_{xy}$ ) and  $\kappa_{xy}$ , and  $\Omega^2$  is the vector composed of all the multiplied combinations of the  $\Omega$  components. The total number of library functions was thus  $N_\Theta = 26$ .

method	$\alpha$	equations
STRidge	$1 \times 10^{-3}$	$\dot{C}_{xx} = +0.410 + 0.078C_{xx} + 0.495(C_{yy} + C_{zz}) - 0.011C_{xx}(C_{yy} + C_{zz}) - 0.092C_{yy}^2 - 0.092C_{zz}^2$ $- 0.092C_{yy}C_{zz} + 2.000C_{xy}\kappa_{xy} - 1.038f_{\text{FENE}}C_{xx} + 0.418f_{\text{FENE}}(C_{yy} + C_{zz})$
		$\dot{C}_{yy} = +0.970 + 0.573(C_{yy} + C_{zz}) - 0.003C_{xx}C_{yy} - 0.002C_{xx}C_{zz} - 0.080C_{yy}^2 - 0.080C_{zz}^2$ $- 0.080C_{yy}C_{zz} - 0.312f_{\text{FENE}}(C_{yy} + C_{zz})$
		$\dot{C}_{zz} = \dot{C}_{yy}$
		$\dot{C}_{xy} = +0.500(C_{yy} + C_{zz})\kappa_{xy} - 1.000f_{\text{FENE}}C_{xy}$
STRidge	$1 \times 10^{-1}$	$\dot{C}_{xx} = +3.333 + 2.000C_{xy}\kappa_{xy} - 1.000f_{\text{FENE}}C_{xx}$
		$\dot{C}_{yy} = +3.326 - 0.499f_{\text{FENE}}(C_{yy} + C_{zz})$
		$\dot{C}_{zz} = \dot{C}_{yy}$
		$\dot{C}_{xy} = +0.500(C_{yy} + C_{zz})\kappa_{xy} - 1.000f_{\text{FENE}}C_{xy}$
a-Lasso	$1 \times 10^{-7}$	$\dot{C}_{xx} = -0.208C_{xx} + 0.436C_{yy} - 0.042C_{xx}C_{yy} + 1.946C_{xy}\kappa_{xy} + 0.072\kappa_{xy}^2$ $- 0.683f_{\text{FENE}}C_{xx} + 0.683f_{\text{FENE}}C_{yy}$
		$\dot{C}_{yy} = 0$
		$\dot{C}_{zz} = \dot{C}_{yy}$
		$\dot{C}_{xy} = +1.101\kappa_{xy} - 0.017C_{xx}C_{xy} - 0.086C_{yy}C_{xy} + 0.314C_{yy}\kappa_{xy} - 0.107C_{zz}C_{xy} + 0.210C_{zz}\kappa_{xy}$ $- 0.289f_{\text{FENE}}C_{xy} + 0.424f_{\text{FENE}}\kappa_{xy}$
a-Lasso	$1 \times 10^{-4}$	$\dot{C}_{xx} = +1.977C_{xy}\kappa_{xy} - 0.998f_{\text{FENE}}C_{xx} + 1.007f_{\text{FENE}}C_{yy}$
		$\dot{C}_{yy} = 0$
		$\dot{C}_{zz} = \dot{C}_{yy}$
		$\dot{C}_{xy} = +3.219\kappa_{xy} - 1.005f_{\text{FENE}}C_{xy}$

FIG. 5. The constitutive equations obtained by *Rheo-SINDy* with the STRidge and a-Lasso for the FENE-P dumbbell model in conformation expression (Eqs. (24)–(26) with  $n_K = 10$ ).

Figure 4 displays the results: (a) the total number of predicted terms and (b) the error rate as a function of the hyperparameter  $\alpha$ . The error rate is defined as the sum of the mean squared errors (MSEs) of  $\hat{t}_{\mu\nu} - \Theta \hat{\xi}_{\mu\nu}$  scaled so that the maximum value of each method is 1. Similar to the results for the phenomenological constitutive equations shown in Sec. S3 in the supplementary material, the a-Lasso provides sparser solutions than the STRidge, and the STRidge gives lower error rates than the a-Lasso. Figure 5 presents the differential equations obtained by the STRidge and a-Lasso for two  $\alpha$  values that yield the nearly correct number of terms with a small error rate. From the lower part of Fig. 5, while the a-Lasso can provide sparser solutions, they are not correct (cf. Eqs. (24)–(26)). Specifically, in all cases for  $C_{xx}$ ,  $C_{yy}$ , and  $C_{zz}$ , the a-Lasso failed to identify the constant term in Eqs. (24) and (25), which is a possible source of larger errors compared to the STRidge. In the case of the STRidge, we confirmed that by choosing the appropriate  $\alpha$  ( $\alpha = 1 \times 10^{-1}$ ), nearly correct differential equations can be obtained, as shown in the upper part of Fig. 5. Since the  $yy$ -component and  $zz$ -component of the stress are equivalent, the exact equations can be recovered by setting  $C_{yy} = C_{zz}$ . Thus, we conclude that the correct differential equations for the FENE-P dumbbell model can be obtained by *Rheo-SINDy* if we properly prepare the library functions and tune the hyperparameter.

To validate the obtained equations in Fig. 5, we generated data using the equations under conditions different from those used to generate the training data (namely, the oscillatory shear flow with  $\gamma_0 = 4$  and  $\omega = 1$ ), and converted

these data to the stress data using the dimensionless form of Eq. (23). Figure 6 compares the generated data with the correct data generated from Eqs. (23)–(26). As shown in this figure, the equations obtained by the STRidge can reproduce the exact solutions even when the equations are not exactly correct ( $\alpha = 1 \times 10^{-3}$ ). In contrast, the test simulations with the differential equations obtained by the a-Lasso show the deviations from the test data, especially for  $\tau_{xx}$ . These results emphasize the need to choose an appropriate optimization method to obtain reasonable solutions.

We then examine whether the stress expression of the constitutive equation for the FENE-P dumbbell model (cf. Eqs. (29)–(31)) can be found by *Rheo-SINDy*. For such a purpose, we prepared the following custom library:

$$\Theta = \begin{bmatrix} 1 & \{\text{tr}\boldsymbol{\tau}(t_1)\}^p T_s(t_1) & \{\text{tr}\boldsymbol{\tau}(t_1)\}^2 & \{T_s(t_1)\}^p \kappa_{xy}(t_1) \\ 1 & \{\text{tr}\boldsymbol{\tau}(t_2)\}^p T_s(t_2) & \{\text{tr}\boldsymbol{\tau}(t_2)\}^2 & \{T_s(t_2)\}^p \kappa_{xy}(t_2) \\ \vdots & \vdots & \vdots & \vdots \\ 1 & \{\text{tr}\boldsymbol{\tau}(t_n)\}^p T_s(t_n) & \{\text{tr}\boldsymbol{\tau}(t_n)\}^2 & \{T_s(t_n)\}^p \kappa_{xy}(t_n) \end{bmatrix}, \quad (33)$$

where  $T_s$  includes  $\{\tau_{xx}, \tau_{yy}, \tau_{zz}, \tau_{xy}\}$  and  $p$  ( $= 0, 1, 2$ ) is the polynomial order. Thus, the total number of library functions was  $N_\Theta = 29$ . We designed the library to include all terms present in Eqs. (29)–(31). Moreover, we excluded terms that could potentially become large, such as higher-order terms involving  $\kappa_{xy}$ . When such terms are included in the solutions, the differential equations may be unstable, and in worse cases, they may diverge. Furthermore, as proposed by Lennon and coworkers, the principle of frame-invariance can also be used

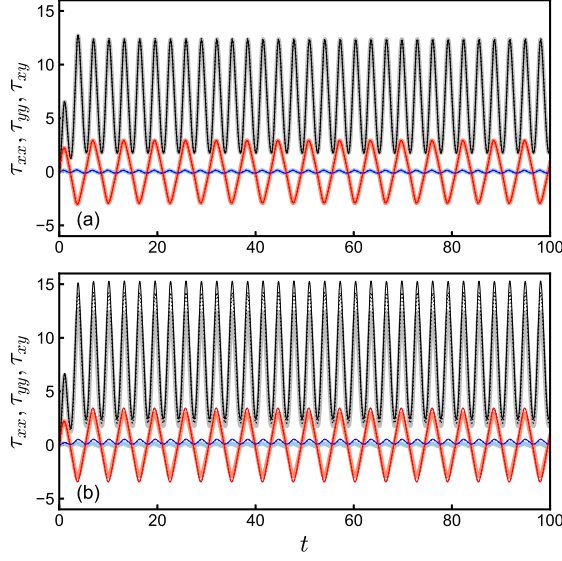


FIG. 6. Test simulation results under the oscillatory shear flow with  $\gamma_0 = 4$  and  $\omega = 1$  using the equations obtained by *Rheo-SINDy* with (a) the STRidge and (b) a-Lasso for the FENE-P dumbbell model in conformation expression. The obtained data from the equations were converted to the stress using the dimensionless form of Eq. (23). The black, blue, and red lines show  $\tau_{xx}$ ,  $\tau_{yy}$ , and  $\tau_{xy}$ . The bold, thin dotted, and thin solid lines indicate the exact solutions (Eqs. (23)–(26) with  $n_K = 10$ ), predictions with smaller  $\alpha$  values ( $\alpha = 1 \times 10^{-3}$  for the STRidge and  $\alpha = 1 \times 10^{-7}$  for the a-Lasso), and predictions with larger  $\alpha$  values ( $\alpha = 1 \times 10^{-1}$  for the STRidge and  $\alpha = 1 \times 10^{-4}$  for the a-Lasso).

to constrain the candidate terms in  $\Theta^{31}$ , which will be considered in our future work.

Figure 7 shows (a) the total number of terms and (b) the error rate of the constitutive equation obtained by *Rheo-SINDy* with the STRidge and a-Lasso for the FENE-P dumbbell model. Similar to the previous case, the a-Lasso yields sparser solutions than the STRidge. Based on the number of terms and the error rates shown in Fig. 7, we chose several  $\alpha$  values with a small number of terms and a low error rate. Figure 8 presents the equations obtained using the chosen  $\alpha$ . From Fig. 8, the equations predicted by the STRidge with  $\alpha = 1$  and the a-Lasso with  $\alpha = 1 \times 10^{-4}$  are almost the same; conversely, the solutions for small  $\alpha$  values significantly differ between the two methods. For the STRidge with  $\alpha = 1 \times 10^{-3}$ , the identified equations are close to the correct equations (cf. Eqs. (29)–(31)). Furthermore, the coefficient values for the terms obtained correctly are close to the correct values. For the a-Lasso with  $\alpha = 1 \times 10^{-8}$ , several coefficients for the correctly obtained terms, such as  $\tau_{xx}$ ,  $\tau_{xy} \kappa_{xy}$ , and  $\tau_{xx} \tau_{xy} \kappa_{xy}$  in the equation for  $\dot{\tau}_{xx}$ , are close to the exact values, but for other several terms, such as  $\text{tr} \tau \tau_{xx}$  in the equation for  $\dot{\tau}_{xx}$ , the correct coefficient values are not obtained. Nevertheless, from Fig. 9, which shows the test simulation results, the equations obtained by the STRidge with  $\alpha = 1 \times 10^{-3}$  and the a-Lasso with  $\alpha = 1 \times 10^{-8}$  can well reproduce the exact solutions including the small oscillation of  $\tau_{yy}$ . Although the equations obtained

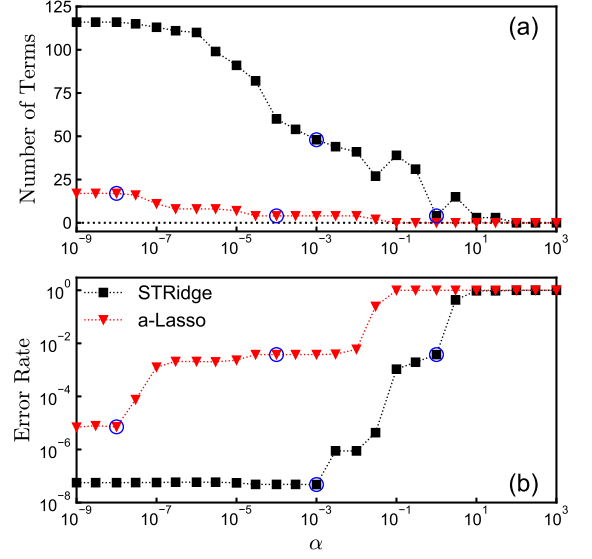


FIG. 7. (a) The total number of terms and (b) the error rate of the constitutive equation obtained by *Rheo-SINDy* with the STRidge (black squares) and the a-Lasso (red reverse triangles) for the FENE-P dumbbell model in stress expression (Eqs. (29)–(31) with  $n_K = 10$ ). The horizontal short-dashed line in (a) indicates that the number of terms is zero. The blue circles represent the  $\alpha$  values selected for test simulations.

TABLE I. The mean squared errors (MSEs) between the predicted and correct constitutive equations for the FENE-P dumbbell model in the stress expression (Eqs. (29)–(31) with  $n_K = 10$ )

method	$\alpha$	MSE ( $\tau_{xx}$ )	MSE ( $\tau_{yy}$ )	MSE ( $\tau_{xy}$ )
STRidge	$1 \times 10^{-3}$	$8.1 \times 10^{-3}$	$3.1 \times 10^{-4}$	$1.1 \times 10^{-3}$
STRidge	1	2.3	$8.2 \times 10^{-3}$	$8.9 \times 10^{-2}$
a-Lasso	$1 \times 10^{-8}$	$3.2 \times 10^{-1}$	$3.4 \times 10^{-3}$	$2.1 \times 10^{-2}$
a-Lasso	$1 \times 10^{-4}$	2.3	$8.2 \times 10^{-3}$	$9.0 \times 10^{-2}$

by the STRidge and a-Lasso demonstrate similar performance in the test simulations shown in Fig. 9, the difference in predictions is quantified by their MSEs shown in Table I. When  $\alpha$  is small, for predictions of  $\tau_{xx}$ ,  $\tau_{yy}$ , and  $\tau_{xy}$ , the STRidge outperforms the a-Lasso. The STRidge, however, generally provides sparse solutions within a narrow range of  $\alpha$  values, requiring careful selection of  $\alpha$ .

### C. FENE Dumbbell Model

Finally, we address the FENE dumbbell model. As explained in Sec. III C, the FENE dumbbell model does not have an analytical expression of the constitutive equation. Thus, we here aim to identify an *approximate* constitutive equation using *Rheo-SINDy*.

To prepare the library  $\Theta$  for the FENE dumbbell model, we utilize the physical insights obtained from the analytical expression of the FENE-P dumbbell model. We here assume the constitutive equation for the FENE-P dumbbell model is *sim-*



method	$\alpha$	equations
STRidge	$1 \times 10^{-3}$	$\dot{\tau}_{xx} = -1.037\tau_{xx} - 0.034(\tau_{yy} + \tau_{zz}) - 0.054\text{tr}\boldsymbol{\tau}\tau_{xx} + 0.018\text{tr}\boldsymbol{\tau}(\tau_{yy} + \tau_{zz}) + 2.074\tau_{xy}\kappa_{xy}$ $- 0.018(\text{tr}\boldsymbol{\tau})^2 - 0.001(\text{tr}\boldsymbol{\tau})^2\tau_{xx} + 0.074\tau_{xx}\tau_{xy}\kappa_{xy} - 0.002(\tau_{yy} + \tau_{zz})\tau_{xy}\kappa_{xy}$
		$\dot{\tau}_{yy} = -0.037\tau_{xx} - 0.530(\tau_{yy} + \tau_{zz}) + 0.022\text{tr}\boldsymbol{\tau}\tau_{xx} - 0.022\text{tr}\boldsymbol{\tau}(\tau_{yy} + \tau_{zz}) + 0.074\tau_{xy}\kappa_{xy}$ $- 0.023(\text{tr}\boldsymbol{\tau})^2 + 0.002(\text{tr}\boldsymbol{\tau})^2(\tau_{yy} + \tau_{zz}) + 0.037(\tau_{yy} + \tau_{zz})\tau_{xy}\kappa_{xy}$
		$\dot{\tau}_{zz} = \dot{\tau}_{yy}$
		$\dot{\tau}_{xy} = -1.000\tau_{xy} + 1.000\kappa_{xy} - 0.070\text{tr}\boldsymbol{\tau}\tau_{xy} + 0.493(\tau_{yy} + \tau_{zz})\kappa_{xy} - 0.001(\text{tr}\boldsymbol{\tau})^2\tau_{xy}$ $+ 0.002\tau_{xx}(\tau_{yy} + \tau_{zz})\kappa_{xy} - 0.014(\tau_{yy}^2 + \tau_{yy}\tau_{zz} + \tau_{zz}^2)\kappa_{xy} + 0.074\tau_{xy}^2\kappa_{xy}$
STRidge	1	$\dot{\tau}_{xx} = -1.173\tau_{xx} + 2.185\tau_{xy}\kappa_{xy}$
		$\dot{\tau}_{yy} = 0$
		$\dot{\tau}_{zz} = \dot{\tau}_{yy}$
		$\dot{\tau}_{xy} = -1.071\tau_{xy} + 1.033\kappa_{xy}$
a-Lasso	$1 \times 10^{-8}$	$\dot{\tau}_{xx} = -1.024\tau_{xx} + 0.424\text{tr}\boldsymbol{\tau}\tau_{xx} + 1.115\text{tr}\boldsymbol{\tau}\tau_{yy} + 2.067\tau_{xy}\kappa_{xy} - 0.504(\text{tr}\boldsymbol{\tau})^2 + 0.075\tau_{xx}\tau_{xy}\kappa_{xy}$
		$\dot{\tau}_{yy} = -0.040\tau_{xx} - 1.182\tau_{yy} + 0.074\tau_{xy}\kappa_{xy}$
		$\dot{\tau}_{zz} = \dot{\tau}_{yy}$
		$\dot{\tau}_{xy} = -0.988\tau_{xy} + 1.001\kappa_{xy} - 0.074\text{tr}\boldsymbol{\tau}\tau_{xy} + 1.025\tau_{yy}\kappa_{xy} + 0.073\tau_{xy}^2\kappa_{xy}$
a-Lasso	$1 \times 10^{-4}$	$\dot{\tau}_{xx} = -1.173\tau_{xx} + 2.185\tau_{xy}\kappa_{xy}$
		$\dot{\tau}_{yy} = 0$
		$\dot{\tau}_{zz} = \dot{\tau}_{yy}$
		$\dot{\tau}_{xy} = -1.070\tau_{xy} + 1.032\kappa_{xy}$

FIG. 8. The constitutive equations obtained by *Rheo-SINDy* with the STRidge and a-Lasso for the FENE-P dumbbell model in stress expression (Eqs. (29)–(31) with  $n_K = 10$ ).

ilar to that for the FENE dumbbell model. Since the FENE-P dumbbell model is a simplified version of the FENE dumbbell model, we believe that this is a reasonable assumption. Here, we note that the stress expression shown in Eq. (23) is no longer applicable to the FENE dumbbell model since the values of  $h(t)$  differ for each individual dumbbell. Thus, it is invalid to obtain stress through the conformation tensor  $\mathbf{C}$ . Based on the above considerations, we decided to use the custom library presented in Eq. (33), which was also used to discover the constitutive equation for the FENE-P dumbbell model.

Figure 10 compares (a) the total number of terms and (b) the error rate predicted by the STRidge and a-Lasso. Similar to the previous discussions, we obtain sparse solutions over a wide range of  $\alpha$  values with the a-Lasso, whereas the STRidge gives sparse solutions only within a limited range of  $\alpha$ . The left table in Fig. 11 shows the equations obtained by the a-Lasso with two  $\alpha$  values chosen from the viewpoints of the sparsity and error rate in the same way as Fig. 7. We note that the predictions obtained by the STRidge are inferior to those obtained by the a-Lasso shown in Fig. 11, which is discussed in Sec. S6 in the supplementary material. From the left table in Fig. 11, if  $\alpha$  is appropriately chosen, the a-Lasso can give sparse equations with coefficients of reasonable (not excessively large) magnitudes. Comparing the equations for the FENE-P model obtained by the a-Lasso with  $\alpha = 1 \times 10^{-8}$  (Fig. 8) and those for the FENE model obtained by the a-Lasso with  $\alpha = 1 \times 10^{-6}$  (Fig. 11), the appearing terms are almost identical, which demonstrates the similarity between

these models. The difference in the coefficients thus represents the difference between these models. The right panels in Fig. 11 show the test simulation results obtained by the equations shown in the left table. We found that the equations obtained with  $\alpha = 1 \times 10^{-6}$  can reproduce well the BD simulation results outside the range of the training data within the investigated parameters, including the oscillatory behavior of  $\tau_{yy}$ . With the large  $\alpha$  ( $\alpha = 3 \times 10^{-4}$ ), the identified equation for  $\tau_{yy}$  becomes  $\dot{\tau}_{yy} = 0$ , which fails to reproduce the oscillatory behavior of  $\tau_{yy}$ . This success suggests that *Rheo-SINDy* with the a-Lasso is effective for discovering *unknown* constitutive equations. Nevertheless, we note that the equations presented in Fig. 11 may fail to predict test data significantly outside the range of the training data. Reproducing such highly nonlinear data would require the nonlinear terms dropped in Fig. 11. In this sense, the constitutive equations for the FENE dumbbell model obtained here are appropriately referred to as the *approximate* constitutive equations.

To further investigate rheological quantities under shear flow, we conducted shear simulations under constant shear rates. Figure 12 compares the steady state shear viscosity  $\eta \equiv \sigma_{xy}/\dot{\gamma}$  and first normal stress coefficient  $\Psi_1 \equiv (\sigma_{xx} - \sigma_{yy})/\dot{\gamma}^2$  obtained from BD simulations with those predicted by *Rheo-SINDy*. Although the constant shear flows considered in Fig. 12 differ from the oscillatory shear flows used to generate the training data, *Rheo-SINDy* can reproduce the results of BD simulations, including shear thinning, within the shear rate region of the training data and slightly beyond it, as shown in Fig. 12(a). However, in the high shear rate region, the *Rheo-*

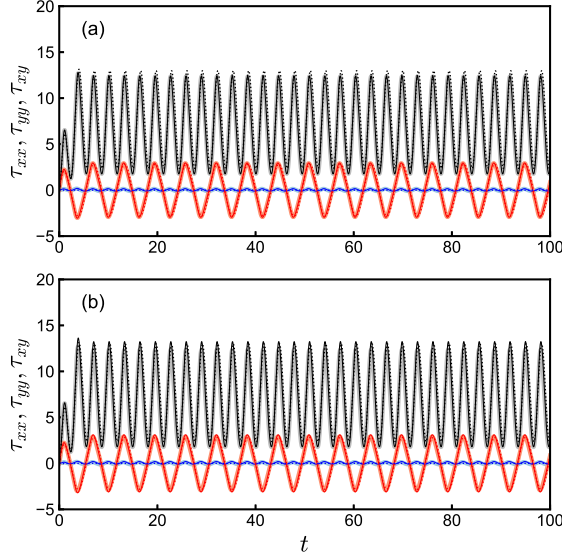


FIG. 9. Test simulation results under the oscillatory shear flow with  $\gamma_0 = 4$  and  $\omega = 1$  using the constitutive equations obtained by *Rheo-SINDy* with (a) the STRidge and (b) a-Lasso for the FENE-P dumbbell model in stress expression. The black, blue, and red lines represent the  $xx$ -,  $yy$ -, and  $xy$ -components of the stress tensor, respectively. The bold lines show the exact solutions. The thin solid and short-dashed lines indicate the results with smaller  $\alpha$  values ( $\alpha = 1 \times 10^{-3}$  for the STRidge and  $\alpha = 1 \times 10^{-8}$  for the a-Lasso) and with larger  $\alpha$  values ( $\alpha = 1$  for the STRidge and  $\alpha = 1 \times 10^{-4}$  for the a-Lasso).

SINDy predictions with  $\alpha = 1 \times 10^{-6}$  exhibit plateaus for  $\eta$  and  $\Psi_1$  that differ from the results of BD simulations. To improve the *Rheo-SINDy* predictions in the high shear rate region, we tested the training data with larger  $\gamma_0$  ( $\gamma_0 = 8$ ) while keeping the same  $\omega$  values as those used to obtain Figs. 10 and 11. We note that the generated data with  $\gamma_0 = 8$  show nonlinear stress responses, as shown in Sec. S7 in the supplementary material. Figure 12(b) indicates that the model found by *Rheo-SINDy* with the training data that includes higher shear rates successfully extrapolates continuous shear thinning to the high shear rate regime beyond the training data.

Thanks to the equations obtained using *Rheo-SINDy*, it is possible to provide a physical interpretation with the assistance of rheological knowledge. For example, from the comparison of the equations obtained for the FENE-P dumbbell model (cf. Fig. 8) and those for the FENE dumbbell model (cf. Fig. 11), the equations for larger  $\alpha$  value ( $\alpha = 1 \times 10^{-4}$  for the FENE-P dumbbell model and  $\alpha = 3 \times 10^{-4}$  for the FENE dumbbell model) are similar except for the coefficient values. Furthermore, the terms in these equations are the same as those for the UCM model (and thus the Hookean dumbbell model). This indicates that all of these models share the same origin based on the dumbbell model. We can also discuss the linear term of stress, which represents the relaxation of stress (see Eq. (S5) in the supplementary material). Since the relaxation time at equilibrium ( $\lambda = \zeta/4h_{eq}$ ) is taken as the unit time in this study, the coefficient of this term should be  $-1$  at equilibrium (and thus for the UCM model, see Eqs. (S6)–

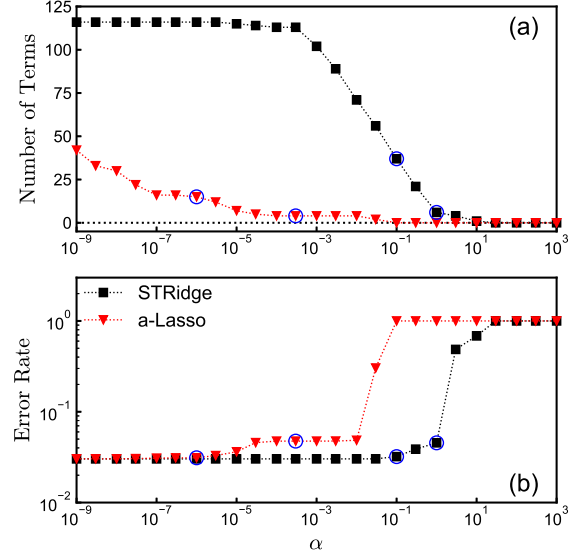


FIG. 10. (a) The total number of terms and (b) the error rate of the constitutive equation obtained by *Rheo-SINDy* with the STRidge (black squares) and the a-Lasso (red reverse triangles) for the FENE dumbbell model. The horizontal short-dashed line in (a) indicates that the number of terms is zero. The blue circles represent the  $\alpha$  values selected for test simulations.

(S8)). From Figs. 8 and 11, the coefficient of the linear term of stress with the larger  $\alpha$  values is smaller than  $-1$ , which indicates  $\lambda_{sf} < \lambda_{eq}$  with the subscript “sf” and “eq” standing for “shear flow” and “equilibrium”, respectively. This indicates that under shear flow, the values of spring strength for the FENE-P and FENE dumbbell models become larger than  $h_{eq}$ , which implies the appearance of the FENE effects under flow. From this discussion, it is evident that *Rheo-SINDy* can provide physically interpretable constitutive equations.

## V. CONCLUDING REMARKS

We tested that the sparse identification for nonlinear dynamics (SINDy) modified for nonlinear rheological data, which we call *Rheo-SINDy*, is effective in finding constitutive equations of complex fluid dynamics. We found that *Rheo-SINDy* can successfully identify correct equations from training data generated from *known* constitutive equations, as well as provide approximate constitutive equations (or reduced order models) from training data generated by mesoscopic models when constitutive equations are analytically *unknown*.

*Rheo-SINDy* for two phenomenological constitutive equations (i.e., the upper convected Maxwell model and Giesekus model) revealed the following two things. First, compared to constant shear tests, oscillatory shear tests are appropriate for generating training data. Second, the sequentially thresholded Ridge regression (STRidge) and adaptive Lasso (a-Lasso) are effective in finding appropriate constitutive equations. We then examined the commonly used mesoscopic model, namely the dumbbell model with three different rep-

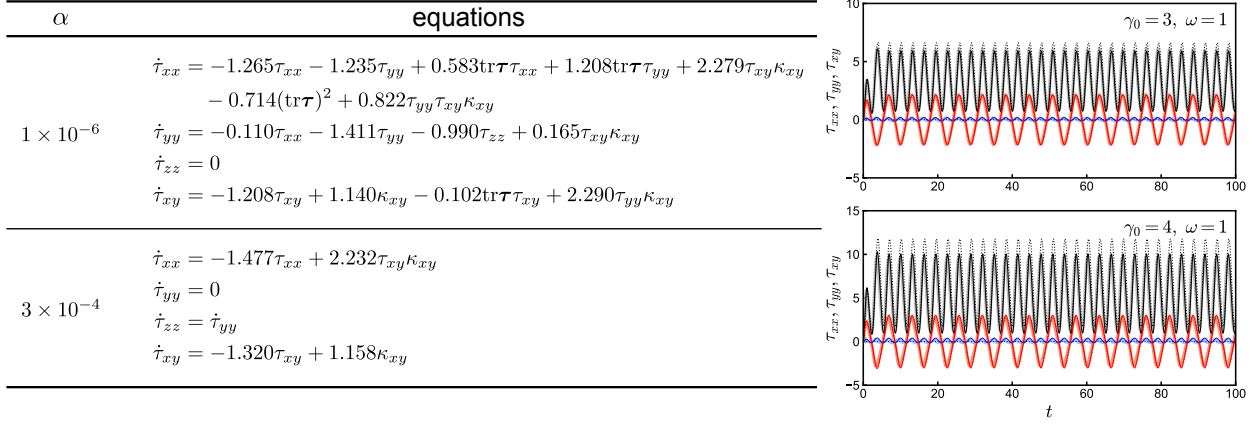


FIG. 11. The constitutive equations obtained by *Rheo-SINDy* with the a-Lasso for the FENE dumbbell model (left) and the test simulation results under the oscillatory shear flows with  $\gamma_0 = 3$  and  $\omega = 1$  (right upper panel) and  $\gamma_0 = 4$  and  $\omega = 1$  (right lower panel). The bold lines show the exact solutions, and the thin solid and short-dashed lines show the results with the smaller  $\alpha$  value ( $\alpha = 1 \times 10^{-6}$ ) and the larger  $\alpha$  value ( $\alpha = 3 \times 10^{-4}$ ).

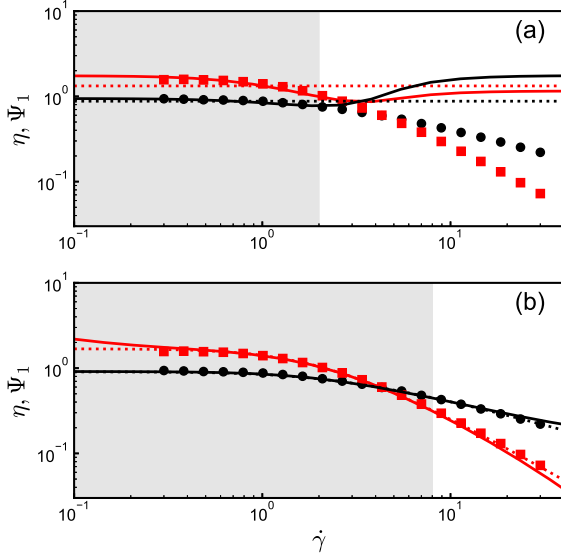


FIG. 12. Steady state shear viscosity  $\eta$  (black) and normal stress coefficient  $\Psi_1$  (red) for the training data (a) with  $\gamma_0 = 2$  and (b) with  $\gamma_0 = 8$ . The symbols are the BD simulation data, and the lines are the *Rheo-SINDy* predictions. The solid and short-dashed lines show the *Rheo-SINDy* results with the smaller  $\alpha$  value ( $\alpha = 1 \times 10^{-6}$  for both (a) and (b)) and the larger  $\alpha$  value ( $\alpha = 3 \times 10^{-4}$  for (a) and  $\alpha = 1 \times 10^{-5}$  for (b)). The shaded regions show the ranges of shear rates in the training data.

representations of spring strength: the Hookean, FENE-P, and FENE springs. Although the Hookean and FENE-P dumbbell models have analytical constitutive equations, for the FENE dumbbell model, there is no analytical expression of the constitutive equation. We confirmed through the Hookean dumbbell model that even in the presence of noise, the a-Lasso provides the correct solution over a wide range of the hyperparameter  $\alpha$ . *Rheo-SINDy* was also effective in discover-

ing the complex constitutive equations for the FENE-P dumbbell model. This case study revealed that the identification of complex equations requires the preparation of an appropriate custom library based on prior physical knowledge. Using physical insights obtained from the Hookean and FENE-P dumbbell models, we attempted to find *approximate* constitutive equations for the FENE dumbbell model. We found that the a-Lasso can successfully give the approximate constitutive equations, which can be used in predictions beyond the range of the training data.

From our investigation, *Rheo-SINDy* with the STRidge or a-Lasso is effective for discovering constitutive equations from nonlinear rheological data. We found that the STRidge is generally superior in terms of retaining correct terms, while the a-Lasso is more robust to the selection of  $\alpha$  than the STRidge. To obtain correct constitutive equations, in addition to selecting the appropriate optimization method, we are required to design an appropriate library by using physical insights, namely *domain knowledge*. Designing such a proper library necessitates not only including necessary terms but also excluding unnecessary terms. For such a purpose, candidate terms can be chosen to satisfy the principle of frame invariance<sup>31</sup>. Furthermore, we may conduct regression with physics-informed constraints on the coefficients<sup>43</sup>.

This research is expected to have an impact on fields such as rheology and fluid mechanics. From a rheological perspective, for several systems such as entangled polymers<sup>44,45</sup> and wormlike micellar solutions<sup>46,47</sup>, sophisticated mesoscopic models suitable for numerical simulations under flow have been proposed. These mesoscopic models can generate reasonable training data not only under shear flow but also under extensional flow. Finding new approximate models from the data obtained by these mesoscopic simulations would be an interesting research subject. Furthermore, it would be desirable to conduct *Rheo-SINDy* for experimental data obtained by Large Amplitude Oscillatory Shear (LAOS) experiments<sup>48</sup>. Since the LAOS measurements do not provide all the major

stress components under shear flow, exploring methods for discovering the constitutive equations from experimental data would be a future challenge. When approximate constitutive models are identified, those models can be employed for predictions of complex flows, which would deepen our understanding of complex fluids. We will continue our research in these directions.

## DATA AVAILABILITY STATEMENT

The data that support the findings of this study are available upon reasonable request from the authors.

## ACKNOWLEDGMENTS

We thank Prof. Yoshinobu Kawahara for his valuable comments on data-driven methods. We also thank Dr. John J. Molina for carefully reading the manuscript and providing insightful comments. TS was partially supported by JST PRESTO Grant Number JPMJPR2203. SM was financially supported by the Kyoto University Science and Technology Innovation Creation Fellowship (FSMAT), Grant Number JPMJFS2123.

## AUTHOR CONTRIBUTIONS

T.S. and S.M. contributed equally to this work.

- <sup>1</sup>S. L. Brunton and J. M. Kutz, *Data-Driven Science and Engineering*, 2nd ed. (Cambridge University Press, 2022).
- <sup>2</sup>S. L. Brunton, J. L. Proctor, and J. N. Kutz, “Discovering governing equations from data by sparse identification of nonlinear dynamical systems,” *Proc. Natl. Acad. Sci. USA* **113**, 3932–3937 (2016).
- <sup>3</sup>B. M. de Silva, D. M. Higdon, S. L. Brunton, and J. N. Kutz, “Discovery of physics from data: Universal laws and discrepancies,” *Front. Artif. Intell.* **3**, 25 (2020).
- <sup>4</sup>K. Kaheman, S. L. Brunton, and J. Nathan Kutz, “Automatic differentiation to simultaneously identify nonlinear dynamics and extract noise probability distributions from data,” *Mach. Learn.: Sci. Technol.* **3**, 015031 (2022).
- <sup>5</sup>U. Fasel, J. N. Kutz, B. W. Brunton, and S. L. Brunton, “Ensemble-SINDy: Robust sparse model discovery in the low-data, high-noise limit, with active learning and control,” *Proc. Math. Phys. Eng. Sci.* **478**, 20210904 (2022).
- <sup>6</sup>M. Schmidt and H. Lipson, “Distilling Free-Form natural laws from experimental data,” *Science* **324**, 81–85 (2009).
- <sup>7</sup>J. Bongard and H. Lipson, “Automated reverse engineering of nonlinear dynamical systems,” *Proc. Natl. Acad. Sci. USA* **104**, 9943–9948 (2007).
- <sup>8</sup>P. A. K. Reinbold, L. M. Kageorge, M. F. Schatz, and R. O. Grigoriev, “Robust learning from noisy, incomplete, high-dimensional experimental data via physically constrained symbolic regression,” *Nat. Commun.* **12**, 3219 (2021).
- <sup>9</sup>S.-M. Udrescu and M. Tegmark, “AI feynman: A physics-inspired method for symbolic regression,” *Sci. Adv.* **6**, eaay2631 (2020).
- <sup>10</sup>M. Cranmer, A. Sanchez Gonzalez, P. Battaglia, R. Xu, K. Cranmer, D. Spergel, and S. Ho, “Discovering symbolic models from deep learning with inductive biases,” in *NeurIPS*, Vol. 33, edited by H. Larochelle, M. Ranzato, R. Hadsell, M. Balcan, and H. Lin (2020) pp. 17429–17442.
- <sup>11</sup>P. Lemos, N. Jeffrey, M. Cranmer, S. Ho, and P. Battaglia, “Rediscovering orbital mechanics with machine learning,” *Mach. Learn.: Sci. Technol.* **4**, 045002 (2023).
- <sup>12</sup>G. E. Karniadakis, I. G. Kevrekidis, L. Lu, P. Perdikaris, S. Wang, and L. Yang, “Physics-informed machine learning,” *Nat. Rev. Phys.* **3**, 422–440 (2021).
- <sup>13</sup>M. Raissi, P. Perdikaris, and G. E. Karniadakis, “Physics-informed neural networks: A deep learning framework for solving forward and inverse problems involving nonlinear partial differential equations,” *Journal of computational physics* **378**, 686–707 (2019).
- <sup>14</sup>X. Jia, J. Willard, A. Karpatne, J. S. Read, J. A. Zwart, M. Steinbach, and V. Kumar, “Physics-Guided machine learning for scientific discovery: An application in simulating lake temperature profiles,” *ACM/IMS Trans. Data Sci.* **2**, 1–26 (2021).
- <sup>15</sup>S. G. Rosofsky, H. Al Majed, and E. A. Huerta, “Applications of physics informed neural operators,” *Machine Learning: Science and Technology* **4**, 025022 (2023).
- <sup>16</sup>R. G. Larson, *Constitutive Equations for Polymer Melts and Solutions* (Butterworths Series in Chemical Engineering, 1988).
- <sup>17</sup>P. E. Rouse, “A Theory of the Linear Viscoelastic Properties of Dilute Solutions of Coiling Polymers,” *J. Chem. Phys.* **21**, 1272–1280 (1953).
- <sup>18</sup>M. Doi and S. F. Edwards, *The Theory of Polymer Dynamics* (Oxford University Press, 1986).
- <sup>19</sup>Y. Masubuchi, J.-I. Takimoto, K. Koyama, G. Ianniruberto, G. Marrucci, and F. Greco, “Brownian simulations of a network of reptating primitive chains,” *J. Chem. Phys.* **115**, 4387–4394 (2001).
- <sup>20</sup>M. Doi and J. Takimoto, “Molecular modelling of entanglement,” *Phil. Trans. R. Soc. A* **361**, 641–652 (2003).
- <sup>21</sup>A. E. Likhtman, “Single-chain slip-link model of entangled polymers: Simultaneous description of neutron spin-echo, rheology, and diffusion,” *Macromolecules* **38**, 6128–6139 (2005).
- <sup>22</sup>S. Jamali, “Data-driven rheology: could be a new paradigm?” *Rheology Bulletin* **92**, 20–24 (2023).
- <sup>23</sup>S. Miyamoto, “Short review on machine learning-based multi-scale simulation in rheology,” *Nihon Reoroji Gakkaishi (J. Soc. Rheol. Jpn.)* **52**, 15–19 (2024).
- <sup>24</sup>L. Fang, P. Ge, L. Zhang, W. E, and H. Lei, “DeePN<sup>2</sup>: a deep learning-based non-newtonian hydrodynamic model,” *J. Mach. Learn.* **1**, 114–140 (2022).
- <sup>25</sup>M. Mahmoudabadbozchelou, K. M. Kamani, S. A. Rogers, and S. Jamali, “Digital rheometer twins: Learning the hidden rheology of complex fluids through rheology-informed graph neural networks,” *Proc. Natl. Acad. Sci. USA* **119**, e2202234119 (2022).
- <sup>26</sup>H. Jin, S. Yoon, F. C. Park, and K. H. Ahn, “Data-driven constitutive model of complex fluids using recurrent neural networks,” *Rheol. Acta* **62**, 569–586 (2023).
- <sup>27</sup>M. Mahmoudabadbozchelou and S. Jamali, “Rheology-informed neural networks (RhINNs) for forward and inverse metamodeling of complex fluids,” *Sci. Rep.* **11**, 12015 (2021).
- <sup>28</sup>M. Mahmoudabadbozchelou, G. E. Karniadakis, and S. Jamali, “nn-PINNs: non-newtonian physics-informed neural networks for complex fluid modeling,” *Soft Matter* **18**, 172–185 (2022).
- <sup>29</sup>M. Saadat, M. Mahmoudabadbozchelou, and S. Jamali, “Data-driven selection of constitutive models via rheology-informed neural networks (RhINNs),” *Rheol. Acta* **61**, 721–732 (2022).
- <sup>30</sup>M. Mahmoudabadbozchelou, M. Caggioni, S. Shahsavari, W. H. Hartt, G. E. Karniadakis, and S. Jamali, “Data-driven physics-informed constitutive metamodeling of complex fluids: A multifidelity neural network (MFNN) framework,” *J. Rheol.* **65**, 179–198 (2021).
- <sup>31</sup>K. R. Lennon, G. H. McKinley, and J. W. Swan, “Scientific machine learning for modeling and simulating complex fluids,” *Proc. Natl. Acad. Sci. USA* **120**, e2304669120 (2023).
- <sup>32</sup>L. Zhao, Z. Li, B. Caswell, J. Ouyang, and G. E. Karniadakis, “Active learning of constitutive relation from mesoscopic dynamics for macroscopic modeling of non-newtonian flows,” *J. Comput. Phys.* **363**, 116–127 (2018).
- <sup>33</sup>L. Zhao, Z. Li, Z. Wang, B. Caswell, J. Ouyang, and G. E. Karniadakis, “Active- and transfer-learning applied to microscale-macroscale coupling to simulate viscoelastic flows,” *J. Comput. Phys.* **427**, 110069 (2021).
- <sup>34</sup>N. Seryo, T. Sato, J. J. Molina, and T. Taniguchi, “Learning the constitutive relation of polymeric flows with memory,” *Phys. Rev. Res.* **2**, 033107 (2020).



- <sup>35</sup>N. Seryo, J. J. Molina, and T. Taniguchi, “Select applications of bayesian data analysis and machine learning to flow problems,” *Nihon Reorogi Gakkaishi (J. Soc. Rheol. Jpn.)* **49**, 97–113 (2021).
- <sup>36</sup>S. Miyamoto, J. J. Molina, and T. Taniguchi, “Machine-learned constitutive relations for multi-scale simulations of well-entangled polymer melts,” *Phys. Fluids* **35**, 063113 (2023).
- <sup>37</sup>K. Fukami, T. Murata, K. Zhang, and K. Fukagata, “Sparse identification of nonlinear dynamics with low-dimensionalized flow representations,” *J. Fluid Mech.* **926**, A10 (2021).
- <sup>38</sup>M. Mahmoudabadbozchelou, K. M. Kamani, S. A. Rogers, and S. Jamali, “Unbiased construction of constitutive relations for soft materials from experiments via rheology-informed neural networks,” *Proc. Natl. Acad. Sci. USA* **121**, e2313658121 (2024).
- <sup>39</sup>R. B. Bird, R. C. Armstrong, and O. Hassager, *Dynamics of Polymeric Liquids*, 2nd ed., Vol. 2 (Oxford University Press, 1987).
- <sup>40</sup>M. Laso and H. Öttinger, “Calculation of viscoelastic flow using molecular models: the connffessit approach,” *J. Non-Newtonian Fluid Mech.* **47**, 1–20 (1993).
- <sup>41</sup>M. D. Graham, “Drag reduction and the dynamics of turbulence in simple and complex fluids,” *Phys. Fluids* **26**, 101301 (2014).
- <sup>42</sup>Y. Mochimaru, “Unsteady-state development of plane couette flow for viscoelastic fluids,” *J. Non-Newtonian Fluid Mech.* **12**, 135–152 (1983).
- <sup>43</sup>J.-C. Loiseau and S. L. Brunton, “Constrained sparse galerkin regression,” *J. Fluid Mech.* **838**, 42–67 (2018).
- <sup>44</sup>T. Sato and T. Taniguchi, “Rheology and entanglement structure of well-entangled polymer melts: A slip-link simulation study,” *Macromolecules* **52**, 3951–3964 (2019).
- <sup>45</sup>S. Miyamoto, T. Sato, and T. Taniguchi, “Stretch-orientation-induced reduction of friction in well-entangled bidisperse blends: a dual slip-link simulation study,” *Rheol. Acta* **62**, 57–70 (2023).
- <sup>46</sup>T. Sato, S. Moghadam, G. Tan, and R. G. Larson, “A slip-spring simulation model for predicting linear and nonlinear rheology of entangled wormlike micellar solutions,” *J. Rheol.* **64**, 1045–1061 (2020).
- <sup>47</sup>T. Sato and R. G. Larson, “Nonlinear rheology of entangled wormlike micellar solutions predicted by a micelle-slip-spring model,” *J. Rheol.* **66**, 639–656 (2022).
- <sup>48</sup>K. Hyun, M. Wilhelm, C. O. Klein, K. S. Cho, J. G. Nam, K. H. Ahn, S. J. Lee, R. H. Ewoldt, and G. H. McKinley, “A review of nonlinear oscillatory shear tests: Analysis and application of large amplitude oscillatory shear (LAOS),” *Prog. Polym. Sci.* **36**, 1697–1753 (2011).

**Rheo-SINDy: Finding a constitutive model from rheological data for complex fluids  
using sparse identification for nonlinear dynamics**

Takeshi Sato,<sup>1, a)</sup> Souta Miyamoto,<sup>2</sup> and Shota Kato<sup>3</sup>

<sup>1)</sup>*Advanced Manufacturing Technology Institute, Kanazawa University,  
Kanazawa 920-1192, Japan*

<sup>2)</sup>*Department of Chemical Engineering, Graduate School of Engineering,  
Kyoto University, Kyoto 615-8510, Japan*

<sup>3)</sup>*Graduate School of Informatics, Kyoto University, Kyoto 606-8501,  
Japan*

(Dated: 7 May 2024)

---

<sup>a)</sup>Electronic mail: takeshis@se.kanazawa-u.ac.jp

## S1. SPARSE REGRESSION METHODS

To solve the optimization problem in Eq. (9) in the main text, we used five sparse regression methods: (i) the sequentially thresholded least squares (STLSQ), (ii) sequentially thresholded Ridge regression (STRidge), (iii) least absolute shrinkage and selection operator (Lasso), (iv) Elastic-Net (E-Net), and (v) adaptive Lasso (a-Lasso).

The differences among these methods lie in the regularization term  $R(\xi_{\mu\nu})$  as shown in Table S1. The hyperparameters of  $\ell_i$  norm ( $i = 0, 1, 2$ ) are denoted as  $\lambda_i$  ( $> 0$ ). The  $\ell_0$  and  $\ell_1$  norms are defined as

$$||\xi_{\mu\nu}||_0 = \sum_j \delta(\xi_{\mu\nu,j}) \quad (\text{S1})$$

and

$$||\xi_{\mu\nu}||_1 = \sum_j |\xi_{\mu\nu,j}|, \quad (\text{S2})$$

where  $\delta(\xi_{\mu\nu,j})$  is the Kronecker delta function, which is equal to 1 if  $\xi_{\mu\nu,j} \neq 0$  and 0 otherwise. The vector  $\xi'_{\mu\nu}$  in the a-Lasso is defined as  $\xi'_{\mu\nu} = \mathbf{w}_{\mu\nu} \otimes \xi_{\mu\nu}$ , where  $\otimes$  is the element-wise product and  $\mathbf{w}_{\mu\nu}$  is the adaptive weight vector and its  $j$ -th element is defined as  $w_{\mu\nu,j} = |\xi_{\mu\nu,j}|^{-\delta}$  with  $\delta$  being the positive constant.

The STLSQ and STRidge were implemented by iteratively conducting the least square regression and the Ridge regression, respectively, while setting the coefficients with smaller absolute values than a certain threshold  $\alpha$  ( $> 0$ ) to zero based on the original papers<sup>S1,S2</sup>. In the STRidge, the hyperparameter  $\lambda_2$  was set to 0.05. The Lasso, E-Net, and a-Lasso were implemented using the scikit-learn library<sup>S3</sup>. In this library, the loss functions for the Lasso and E-Net are respectively

TABLE S1. The regularization term  $R(\xi_{\mu\nu})$  for the sparse regression methods.

Method	Regularization term $R(\xi_{\mu\nu})$
STLSQ	$\lambda_0   \xi_{\mu\nu}  _0$
STRidge	$\lambda_0   \xi_{\mu\nu}  _0 + \lambda_2   \xi_{\mu\nu}  _2^2$
Lasso	$\lambda_1   \xi_{\mu\nu}  _1$
E-Net	$\lambda_1   \xi_{\mu\nu}  _1 + \lambda_2   \xi_{\mu\nu}  _2^2$
a-Lasso	$\lambda_1   \xi'_{\mu\nu}  _1$

defined as

$$\hat{\xi}_{\mu\nu} = \underset{\xi_{\mu\nu}}{\operatorname{argmin}} \frac{1}{2n} \|\dot{t}_{\mu\nu} - \Theta \xi_{\mu\nu}\|_2^2 + \alpha \|\xi_{\mu\nu}\|_1, \quad (\text{S3})$$

and

$$\hat{\xi}_{\mu\nu} = \underset{\xi_{\mu\nu}}{\operatorname{argmin}} \frac{1}{2n} \|\dot{t}_{\mu\nu} - \Theta \xi_{\mu\nu}\|_2^2 + \alpha \beta \|\xi_{\mu\nu}\|_1 + \frac{\alpha(1-\beta)}{2} \|\xi_{\mu\nu}\|_2^2, \quad (\text{S4})$$

where  $n$  is the number of data points,  $\beta$  is the  $\ell_1$  ratio, and  $\alpha$  and  $\beta$  are the hyperparameters. The loss function for the Lasso is obtained by setting  $\beta = 1$  in Eq. (S4). In this study,  $\beta$  was set to 0.5 for the E-Net. According to the original paper of a-Lasso<sup>S4</sup>, the a-Lasso can be implemented as the Lasso problem as the following steps:

1. Define  $\xi'_{\mu\nu,j} = \xi_{\mu\nu,j}/w_{\mu\nu,j}$ ,  $j = 1, \dots, J$ .
2. Solve the Lasso problem for  $\xi'_{\mu\nu}$  using Eq. (S3).
3. Output  $\hat{\xi}_{\mu\nu,j} = \hat{\xi}'_{\mu\nu,j}/w_{\mu\nu,j}$ ,  $j = 1, \dots, J$ .

The adaptive weight  $w_{\mu\nu,j}$  depends on the coefficients, and thereby the output coefficients can be varied in each iteration. To obtain the converged solution, we initialized the weights as unit vectors  $w = 1$  and repeated the above steps until the coefficients  $\hat{\xi}_{\mu\nu,j}$  no longer change<sup>S5</sup>. Here, the hyperparameter  $\delta$  was set to 3 (see Sec. S4 for the effect of  $\delta$ ).

## S2. CASE STUDIES FOR PHENOMENOLOGICAL CONSTITUTIVE EQUATIONS

### A. Upper Convected Maxwell (UCM) Model

The simplest constitutive equation for viscoelastic fluids is the upper convected Maxwell (UCM) model<sup>S6</sup> shown as

$$\frac{d\tau}{dt} - \tau \cdot \kappa^+ - \kappa \cdot \tau = -\frac{1}{\lambda} \tau + 2GD. \quad (\text{S5})$$

Here, the left-hand side of Eq. (S5) is the upper-convected time derivative of  $\tau$ ,  $\lambda$  is the relaxation time,  $G$  is the modulus, and  $D$  is the deformation rate tensor defined as  $D = (\kappa + \kappa^+)/2$ . Using  $\lambda$  as the unit time and  $G$  as the unit stress (i.e.,  $\lambda = G = 1$ ), we can obtain dimensionless expressions for time  $\tilde{t} = t/\lambda$ , velocity gradient tensor  $\tilde{\kappa} = \lambda \kappa$ , and stress  $\tilde{\tau} = \tau/G$ . In what follows, we omit



the tilde in dimensionless variables for simplicity. The dimensionless form of the UCM model under shear flow is thus written as

$$\dot{\tau}_{xx} = -\tau_{xx} + 2\tau_{xy}\kappa_{xy}, \quad (\text{S6})$$

$$\dot{\tau}_{yy/zz} = \tau_{yy/zz} = 0, \quad (\text{S7})$$

$$\dot{\tau}_{xy} = -\tau_{xy} + \kappa_{xy} + \tau_{yy}\kappa_{xy} = -\tau_{xy} + \kappa_{xy}. \quad (\text{S8})$$

Here, since the initial conditions for  $\tau$  are set to the values of  $\tau$  at equilibrium, namely  $\tau = 0$ ,  $\tau_{yy/zz}$  of the UCM model is zero under shear flow.

For the UCM model, we generate training data by numerically solving Eqs. (S6)–(S8) under two shear flow scenarios: simple shear and oscillatory shear tests. For the simple shear test, the shear rate is kept constant ( $\kappa_{xy} = \dot{\gamma}$ ) across various values ( $\dot{\gamma} \in \{1, 1.7, 2.8, 4.6, 7.7, 13, 22, 36, 60, 100\}$ ) with simulations running from  $t = 0$  to  $t = 10$  using a time step of  $\Delta t = 1.0 \times 10^{-4}$ . The oscillatory shear test introduces a time-dependent oscillatory shear strain,  $\gamma(t) = \gamma_0 \sin(\omega t)$ , with  $\gamma_0 = 2$  and  $\omega = 1$ , over a period from  $t = 0$  to  $t = 100$ , employing the same time step. In both tests, data are collected at intervals of  $\Delta t_{\text{train}} = 1 \times 10^{-2}$ , resulting in a total of  $10^4$  data points for the training data.

## B. Giesekus Model

The Giesekus model, which is one of the most popular phenomenological constitutive equations<sup>S7</sup>, shows typical shear rheological properties and is used to fit various complex fluids, including polymer solutions and wormlike micellar solutions. The tensorial form of the Giesekus constitutive equation can be written as

$$\frac{d\tau}{dt} - \tau \cdot \kappa^+ - \kappa \cdot \tau = -\frac{1}{\lambda} \tau - \frac{\alpha_G}{G\lambda} \tau \cdot \tau + 2GD, \quad (\text{S9})$$

where  $\alpha_G$  is the parameter governing the nonlinear response of the Giesekus model. The Giesekus equation under shear flow is thus given by

$$\dot{\tau}_{xx} = -\tau_{xx} - \alpha_G(\tau_{xx}^2 + \tau_{xy}^2) + 2\tau_{xy}\kappa_{xy}, \quad (\text{S10})$$

$$\dot{\tau}_{yy} = -\tau_{yy} - \alpha_G(\tau_{yy}^2 + \tau_{xy}^2), \quad (\text{S11})$$

$$\dot{\tau}_{zz} = 0, \quad (\text{S12})$$

$$\dot{\tau}_{xy} = -\tau_{xy} - \alpha_G(\tau_{xx} + \tau_{yy})\tau_{xy} + \tau_{yy}\kappa_{xy} + \kappa_{xy}. \quad (\text{S13})$$

Here, all quantities are non-dimensionalized by using  $\lambda$  as the unit time and  $G$  as the unit stress. From Eqs. (S10)–(S13), the total number of collect terms in the Giesekus model is 12.

We generate the training data by solving Eqs. (S10)–(S13) numerically with  $\alpha_G = 0.5$  and  $\Delta t = 1 \times 10^{-4}$ . We note that the Giesekus model with  $\alpha_G = 0.5$  gives sufficient nonlinear features under shear flow. We applied the oscillatory shear flow with  $\gamma_0 = 2$  and various  $\omega$  values ( $\omega \in \{0.1, 0.2, \dots, 1\}$ ) for  $0 \leq t \leq 100$ . From the computed stress data, we collected data at the interval of  $\Delta t_{\text{train}} = 1 \times 10^{-2}$ .

### S3. RHEO-SINDY RESULTS FOR PHENOMENOLOGICAL CONSTITUTIVE EQUATIONS

#### A. Upper Convected Maxwell Model

Through this case study, we first check the appropriate methods to take the shear rheological data for *Rheo*-SINDy. Figure S1 shows the training data and results for the UCM model. Figure S1(a) and (b) are the stress data under the simple shear flows with the various shear rates and those under the oscillatory shear flow.

We conducted the *Rheo*-SINDy regressions by using the polynomial library that includes up to third order terms of  $\tau_{xx}$ ,  $\tau_{yy}$ ,  $\tau_{xy}$ , and  $\kappa_{xy}$ . Thus, there were 35 candidate terms for each component of the constitutive equation. The terms related to  $\tau_{zz}$  were excluded because they do not contribute to the UCM dynamics. The correct number of terms is four, as shown in Eqs. (S6)–(S8). Figures S1(c) and (d) present the number of total terms varying with the hyperparameter  $\alpha$  obtained by *Rheo*-SINDy using the training data (a) and (b), respectively (for the detail of the hyperparameter  $\alpha$ , see Sec. S1). Figure S1(c) indicates that the sparse solutions can be obtained by the STLSQ, STRidge, and a-Lasso, but not by the Lasso and E-Net. Moreover, regarding the number of terms, the STLSQ and STRidge exhibit similar behavior. Specifically, we confirm that the correct *number* of terms (cf. Eqs. (S6)–(S8)) are obtained by the STLSQ and STRidge with  $3 \times 10^{-3} \leq \alpha \leq 3 \times 10^{-1}$ . Figure S1(d) indicates that the STLSQ, STRidge, and a-Lasso yielded the correct number of terms, though all five methods gave sparse solutions. In most of the cases where the number of terms obtained was correct, the obtained coefficients were also correct for the UCM model. These results suggest that the oscillatory shear test is more appropriate than the simple shear test to obtain the correct constitutive equations for the UCM model. Figure S1(e)

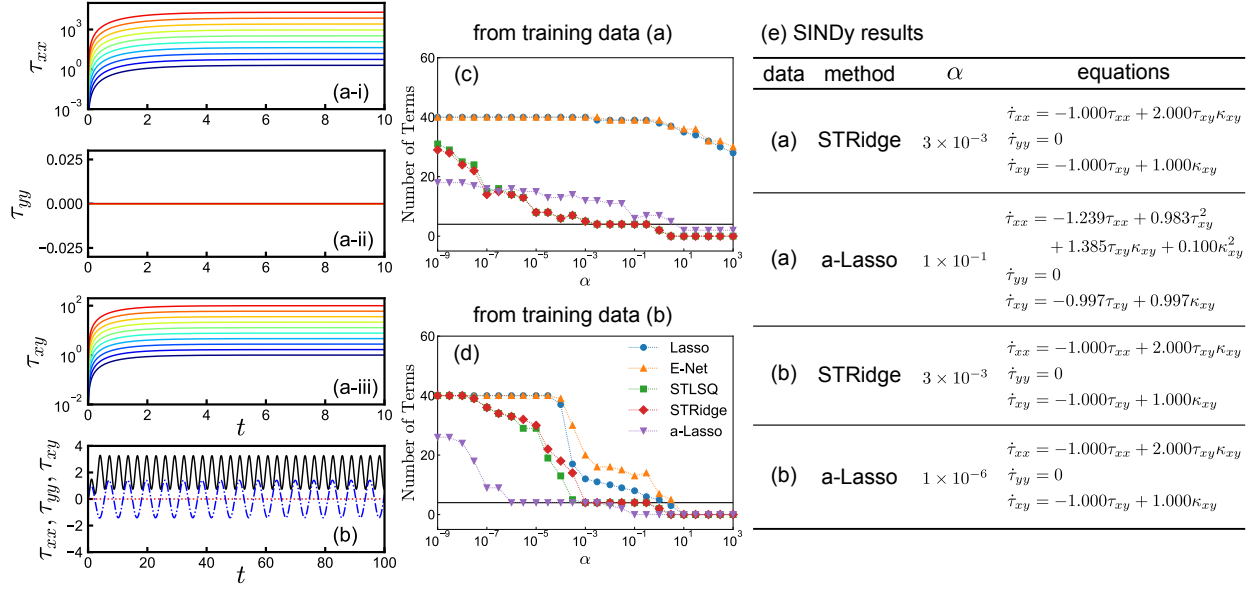


FIG. S1. Training data obtained by the UCM model (a) under simple shear flow ( $\kappa_{xy} = \dot{\gamma}$ ) and (b) under oscillatory shear flow ( $\kappa_{xy} = \gamma_0 \omega \cos(\omega t)$ ). The number of total terms obtained by (c) the training data (a) (i.e., simple shear flow) and by (d) the training data (b) (i.e., oscillatory shear flow). (e) The constitutive equations obtained by *Rheo*-SINDy. Here, the exact equations for the UCM model under shear flow are shown in Eqs. (S6)–(S8). The parameters for the applied shear flows to obtain the training data are summarized in Sec. S2 A. In (b),  $xx$ -,  $yy$ -, and  $xy$ -components of the stress tensor are plotted with the black solid, red dotted, and blue dash-dotted lines, respectively. In (c) and (d), the number of total terms for five different optimization methods is plotted against the hyperparameter  $\alpha$ . The black horizontal lines in (c) and (d) indicate the correct number of the terms in the UCM model.

lists the constitutive equations obtained by the STRidge and a-Lasso. We can see that the STRidge and a-Lasso can give the correct constitutive equations, except for the a-Lasso in the simple shear test. Furthermore, we confirmed that the correct equations were obtained even for  $\alpha$  values not shown in Fig. S1(e) in the case of the UCM model. These findings show the basic validity of finding the constitutive equations from the rheological data by *Rheo*-SINDy. Figure S1 indicates that the STLSQ, STRidge, and a-Lasso demonstrate better performance in discovering the correct constitutive equations compared to the Lasso and E-Net; thus, we use the former three methods in the following discussion.

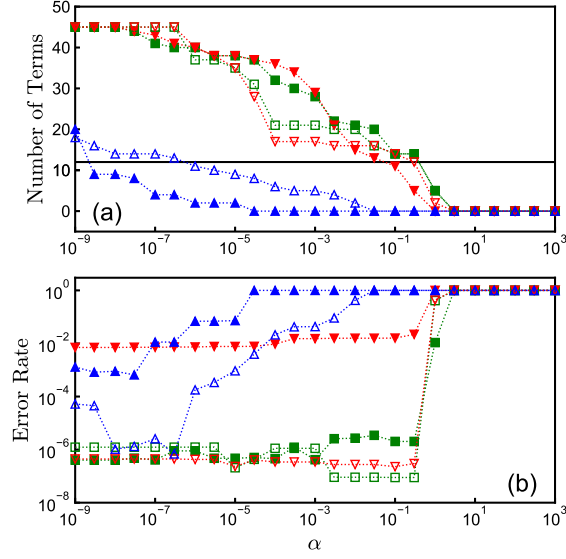


FIG. S2. (a) The number of total terms and (b) the error rate of the constitutive equations obtained by *Rheo*-SINDy for the Giesekus model. The optimization methods include the STLSQ (green squares), STRidge (red reverse triangles), and a-Lasso (blue triangles). The filled and open symbols indicate the results with the single data trajectory of  $\kappa_{xy} = \gamma_0 \omega \cos(\omega t)$  with  $\gamma_0 = 2$  and  $\omega = 0.1$  for  $0 \leq t \leq 100$  and those with the multiple (10) data trajectories of  $\kappa_{xy} = \gamma_0 \omega \cos(\omega t)$  with  $\gamma_0 = 2$  and  $\omega \in \{0.1, 0.2, \dots, 1\}$  for  $0 \leq t \leq 100$ , respectively.

## B. Giesekus Model

We here explain the results of *Rheo*-SINDy for the Giesekus model. This case used the polynomial library consisting of up to second-order terms of  $\tau_{xx}$ ,  $\tau_{yy}$ ,  $\tau_{xy}$ , and  $\kappa_{xy}$ , which is the sufficient candidate terms to obtain the exact equations. Figure S2 shows (a) the total number of terms and (b) the error rate obtained by *Rheo*-SINDy for the training data of the Giesekus model. The error rate is defined as the sum of the mean squared errors (MSEs) of  $\dot{t}_{\mu\nu} - \Theta \hat{\xi}_{\mu\nu}$ . The MSEs were scaled so that the maximum value of each method was 1. We show results using a single data trajectory with  $\omega = 0.1$  and multiple data trajectories with  $\omega \in \{0.1, 0.2, \dots, 1.0\}$  as the training data. Figure S2(a) indicates that the a-Lasso evidently provides a sparser solution compared to the other two methods. Furthermore, Fig. S2(b) demonstrates that the regressions using the multiple data trajectories give solutions with smaller errors than those using the single data trajectory. We note that, similar to the number of terms obtained by *Rheo*-SINDy, coefficient values generally depend on  $\alpha$ .



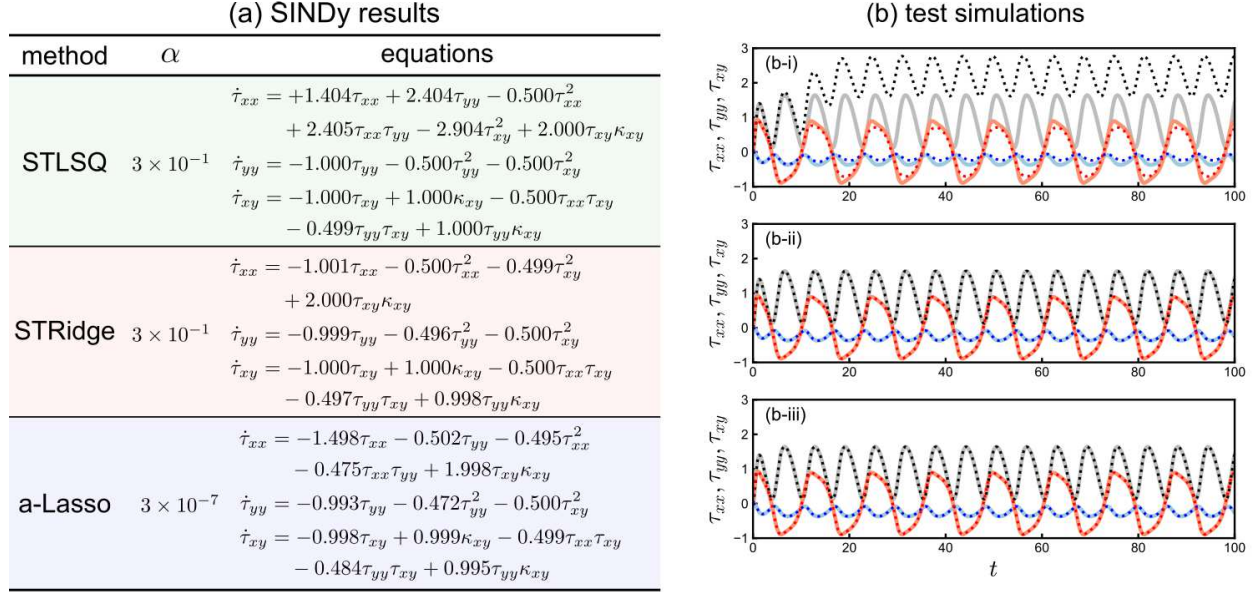


FIG. S3. (a) The constitutive equations obtained by *Rheo*-SINDy with (i) the STLSQ, (ii) STRidge, (iii) and a-Lasso and (b) their test simulation results under the oscillatory shear flow with  $\gamma_0 = 4$  and  $\omega = 0.5$ . The training data are the same as those in Fig. S2. The exact equations for the Giesekus model under shear flow are shown in Eqs. (S10)–(S13). In (a), the constitutive equations obtained by the multiple data trajectories are shown. In (b), the  $xx$ -,  $yy$ -, and  $xy$ -components of the stress tensor are shown with black, blue, and red lines, respectively. The dotted and solid lines in (b) denote the predictions by the equations shown in (a) and those by the exact Giesekus model, respectively.

Figures S3(a) and (b) show the constitutive equations found by *Rheo*-SINDy and the test simulation results, respectively. Here, we used the training data of the multiple data trajectories. The  $\alpha$  value for each method was chosen considering the sparsity indicated in Fig. S2(a) and the small loss indicated in Fig. S2(b). For test simulations shown in Fig. S3(b), we employed the oscillatory shear flow with  $\gamma_0 = 4$  and  $\omega = 0.5$ , which is outside of the parameters in the training data described in Sec. S2 B. Figure S3(a) reveals that the STRidge with  $\alpha = 3 \times 10^{-1}$  can give almost exact constitutive equations, including the value of  $\alpha_G$  (cf. Eqs. (S10)–(S13)). As inferred from this, the predictions based on the constitutive equations obtained by the STRidge demonstrate a good agreement with the test data, as shown in Fig. S3(b-ii). In contrast to the success of the STRidge, the STLSQ and a-Lasso failed to identify the correct solution, as indicated in Fig. S3(a). The constitutive equation obtained by the STLSQ with  $\alpha = 3 \times 10^{-1}$  has a low error rate as shown in Fig. S2(b), but its predicted  $\tau_{xx}$  significantly deviates from the test data as seen in Fig. S3(b-i).

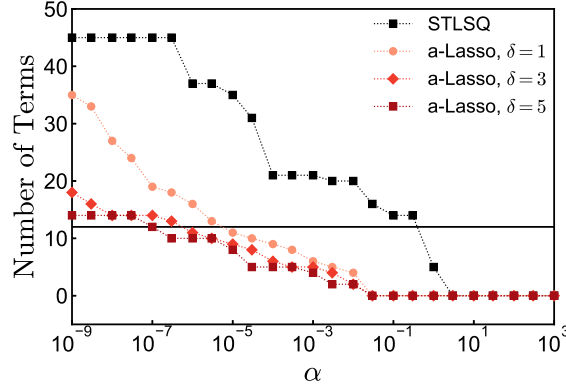


FIG. S4. The total number of terms obtained by *Rheo*-SINDy with the STLSQ (black symbols) and a-Lasso (red symbols) for the Giesekus model. Here, the circles, diamonds, and squares in the red series indicate the results with  $\delta = 1, 3$ , and  $5$  for the adaptive weight  $w_{\mu\nu,j}$ , respectively.

In contrast, although the a-Lasso did not provide the correct solution for  $\tau_{xx}$ , the test simulations with the obtained constitutive equations exhibit a good agreement with the test data. These test simulations demonstrate that the STRidge and a-Lasso are promising approaches for *Rheo*-SINDy.

#### S4. HYPERPARAMETER OF THE ADAPTIVE LASSO

Here, we shortly note the effect of changing the hyperparameter  $\delta$  of the a-Lasso, which determines the adaptive weight. Figure S4 compares the total number of terms for the Giesekus model obtained by the a-Lasso with three different  $\delta$  values. The training data include the multiple trajectories, which are the same as those in Fig. S3. Here, the results for the STLSQ are also shown for comparison. As shown in Fig. S4, the solutions obtained by the a-Lasso with  $\delta = 1, 3$ , and  $5$  are sparser than those obtained by the STLSQ. Due to the increased effects of weights, the solutions for  $\delta = 3$  and  $5$  are sparser compared to the solutions for  $\delta = 1$ . Moreover, the results with  $\delta = 3$  are almost the same as those with  $\delta = 5$ , although the a-Lasso with  $\delta = 5$  provides slightly sparser solutions. Thus, the hyperparameter  $\delta = 3$  can be considered sufficiently large to obtain sparse solutions. We note, in general, that a sparser solution is superior from the perspective of overfitting and helps prevent unexpected divergence during test simulations. From these discussions, in this study, we used  $\delta = 3$  as the adaptive weight in the a-Lasso.

## S5. STRESS EXPRESSIONS FOR THE FENE-P DUMBBELL MODEL

As noted in Sec. 3.3 in the main text, the constitutive equation for the FENE-P dumbbell model can be expressed in terms of the stress (cf. Eqs. (29)–(31)). We here show the derivation of the constitutive equation for the FENE-P model<sup>S8</sup>.

To improve clarity, let us rewrite the stress  $\boldsymbol{\tau}$  in Eq. (15) in the main text as follows:

$$\boldsymbol{\tau}(t) = \rho h_{\text{eq}} Z_{\text{eq}}^{-1} Z \langle \mathbf{R}(t) \mathbf{R}(t) \rangle - G \mathbf{I}, \quad (\text{S14})$$

where  $Z$  has already been defined in Eq. (28) in the main text and  $Z_{\text{eq}}$  indicates  $Z$  at equilibrium. In what follows, we express all variables in dimensionless forms by using the unit time  $\lambda$  and the unit stress  $\rho k_B T$ . Additionally, for simplicity, we omit the tilde representing dimensionless quantities. Taking the trace of both sides of Eq. (S14) and using the relation  $\langle \mathbf{R}^2(t) \rangle = R_{\text{max}}^2 (1 - Z^{-1})$ , we can rewrite  $Z$  as a function of  $\boldsymbol{\tau}$ :

$$Z = 1 + \frac{1}{3n_K Z_{\text{eq}}^{-1}} (\text{tr} \boldsymbol{\tau} + 3). \quad (\text{S15})$$

Taking the convected derivative of  $\boldsymbol{\tau}/Z$ , the time evolution of stress can be expressed as

$$\frac{d\boldsymbol{\tau}}{dt} - \boldsymbol{\tau} \cdot \boldsymbol{\kappa}^+ - \boldsymbol{\kappa} \cdot \boldsymbol{\tau} = -Z_{\text{eq}}^{-1} Z \boldsymbol{\tau} + 2\mathbf{D} + \frac{D \ln Z}{Dt} (\boldsymbol{\tau} + \mathbf{I}), \quad (\text{S16})$$

which is the same as in Eq. (27) in the main text. Since we do not address the spatial gradient in rheological calculations,  $D(\cdots)/Dt$  simply reduces to  $d(\cdots)/dt$ . To obtain Eq. (S16), we used the following relation that can be obtained by Eqs. (22) and (23) in the main text:

$$\frac{d\mathbf{C}}{dt} - \mathbf{C} \cdot \boldsymbol{\kappa}^+ - \boldsymbol{\kappa} \cdot \mathbf{C} = -\frac{n_K}{3} \boldsymbol{\tau}. \quad (\text{S17})$$

From Eq. (S15), the time evolution of  $\ln Z$  can be expressed in terms of  $\text{tr} \boldsymbol{\tau}$  as

$$\frac{d}{dt} \text{tr} \boldsymbol{\tau} = \{ 3n_K Z_{\text{eq}}^{-1} + (\text{tr} \boldsymbol{\tau} + 3) \} \frac{d \ln Z}{dt}. \quad (\text{S18})$$

Furthermore, taking trace of Eq. (S16) and using Eq. (S18), we can have

$$\frac{d \ln Z}{dt} = \frac{1}{3n_K Z_{\text{eq}}^{-1}} \{ -Z_{\text{eq}}^{-1} Z \text{tr} \boldsymbol{\tau} + 2 \text{tr} \mathbf{D} + \text{tr} (\boldsymbol{\tau} \cdot \boldsymbol{\kappa}^+ + \boldsymbol{\kappa} \cdot \boldsymbol{\tau}) \}. \quad (\text{S19})$$

Combining Eqs. (S16) and (S19), we can express the time evolution of  $\boldsymbol{\tau}$  (i.e.,  $\dot{\boldsymbol{\tau}}$ ) as a function of  $\boldsymbol{\tau}$  and  $\boldsymbol{\kappa}$ . Specifically, Eqs. (S16) and (S19) reduce to Eqs. (29)–(31) in the main text under shear flow.

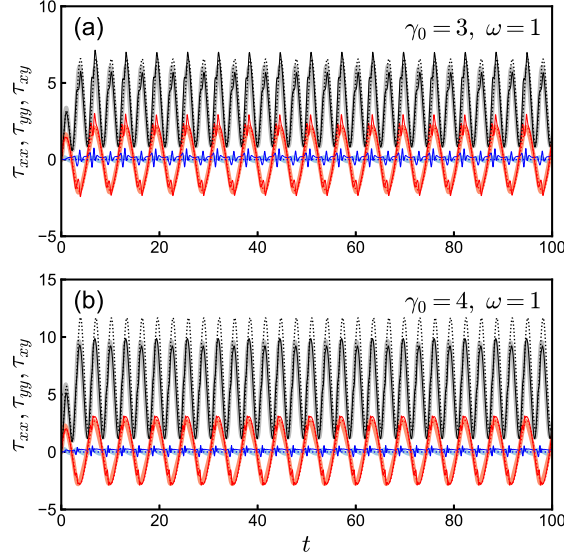


FIG. S5. Test simulation results using equations obtained by *Rheo-SINDy* with the STRidge for the library shown in Eq. (33) in the main text. The test simulations were conducted under the oscillatory shear flows with (a)  $\gamma_0 = 3$  and  $\omega = 1$  and (b)  $\gamma_0 = 4$  and  $\omega = 1$ . The bold lines show the exact solutions, and the thin solid and short-dashed lines show the results with the smaller  $\alpha$  value ( $\alpha = 1 \times 10^{-1}$ ) and the larger  $\alpha$  value ( $\alpha = 1$ ).

## S6. STRIDGE REGRESSIONS FOR THE FENE DUMBBELL MODEL

Figures S5 and S6 show the test simulation results for the FENE dumbbell model using the approximate constitutive equations obtained by *Rheo-SINDy* with the STRidge. Here, in Fig. S5, we employed the custom library shown in Eq. (33) in the main text ( $N_{\Theta} = 29$ ), while in Fig. S6, we utilized a polynomial library including polynomial terms up to the third order of  $\{\tau_{xx}, \tau_{yy}, \tau_{zz}, \tau_{xy}, \kappa_{xy}\}$  ( $N_{\Theta} = 56$ ). From the thin solid lines in Fig. S5, which show the results with the smaller  $\alpha = 1 \times 10^{-1}$ , while the magnitudes of the predicted stress components almost match the results of the BD simulation, spike-like predictions are occasionally observed. When using the third-order polynomial library, the solutions for the small  $\alpha$ , indicated by thin solid lines in Fig. S6, closely resemble the results of the BD simulations. This is likely attributed to the fact that the larger number of candidate terms included in the library improves the predictive ability of the model. Nevertheless, we note that increasing the number of terms in the library without careful consideration does not necessarily lead to an improvement in the model performance. By increasing the number of terms in the library, overfitting issues may arise. For example, when *Rheo-SINDy* chooses terms



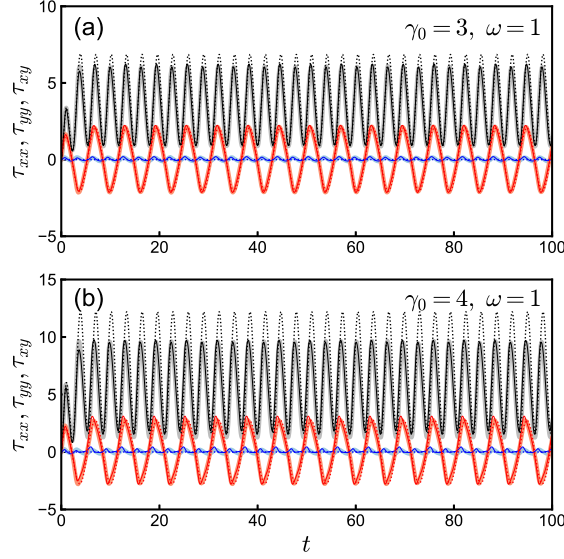


FIG. S6. Test simulation results using equations obtained by *Rheo-SINDy* with the STRidge for the library including polynomial terms up to the third order of  $\{\tau_{xx}, \tau_{yy}, \tau_{zz}, \tau_{xy}, \kappa_{xy}\}$ . The flow parameters for the test simulations are the same as those in Fig. S5. The bold lines show the exact solutions, and the thin solid and short-dashed lines show the results with the smaller  $\alpha$  value ( $\alpha = 3 \times 10^{-2}$ ) and the larger  $\alpha$  value ( $\alpha = 1$ ).

that are likely to be significantly large under shear flow, such as  $\tau_{xx} \kappa_{xy}^2$ , there is an increased possibility that the differential equations may fail to be solved when conducting test simulations for the parameters outside of the training data.

## S7. REGRESSIONS USING THE TRAINING DATA WITH THE LARGE $\gamma_0$

Here, we conducted the *Rheo-SINDy* regressions for the FENE dumbbell model using training data with a larger  $\gamma_0$  value ( $\gamma_0 = 8$ ) than the standard  $\gamma_0$  value ( $\gamma_0 = 2$ ). As shown in Fig. S7, the training data with  $\gamma_0 = 8$  include the nonlinear shear responses.

Figure S8 show the total number of terms and the error rate obtained by *Rheo-SINDy* for the training data with  $\gamma_0 = 8$ . Although the  $\alpha$  dependence of the solutions shows a similar trend to Fig. 10 in the main text, the total number of terms at the same  $\alpha$  is larger for the *Rheo-SINDy* regression using the training data with  $\gamma_0 = 8$  than with  $\gamma_0 = 2$ . In Fig. S9, we show the equations obtained by *Rheo-SINDy* for the two  $\alpha$  values indicated in blue circles in Fig. S8. As shown in Fig. S9, the regression results using the training data generated with  $\gamma_0 = 8$  include nonlinear terms that are not present in Fig. 11 of the main text.

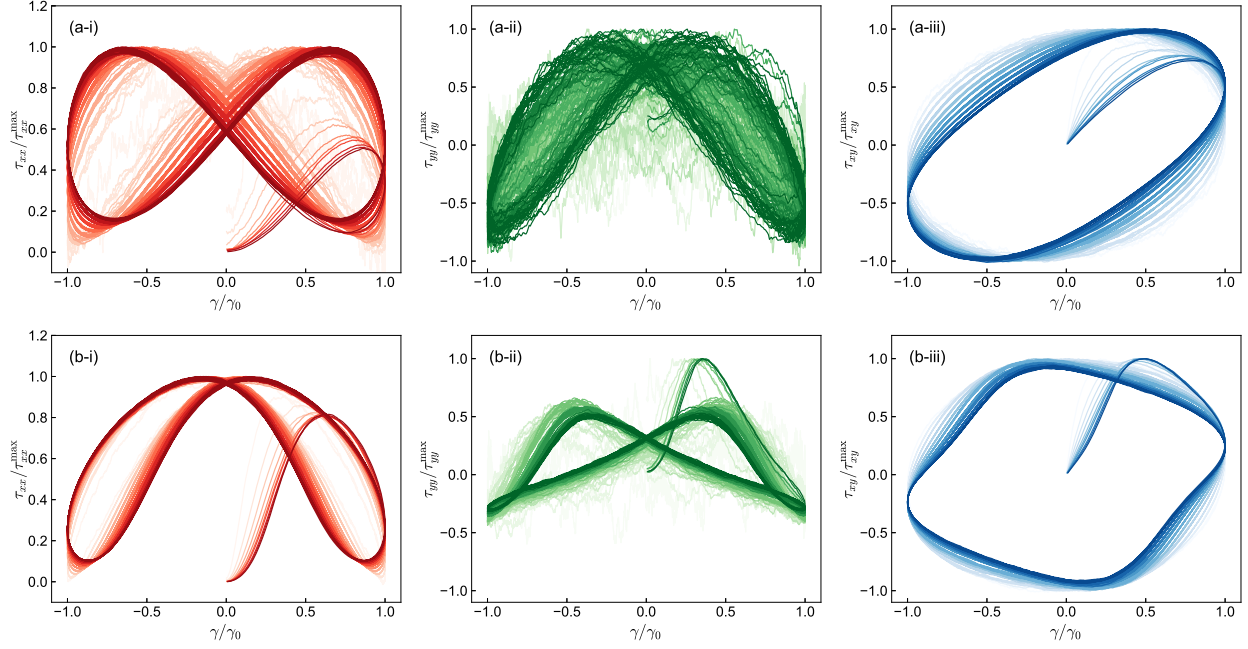


FIG. S7. The normalized training data (a) with the standard  $\gamma_0$  ( $\gamma_0 = 2$ ) and (b) with the larger  $\gamma_0$  ( $\gamma_0 = 8$ ). The different colors in each panel distinguish the different  $\omega$  values ( $\omega \in \{0.1, 0.2, \dots, 1\}$ ).

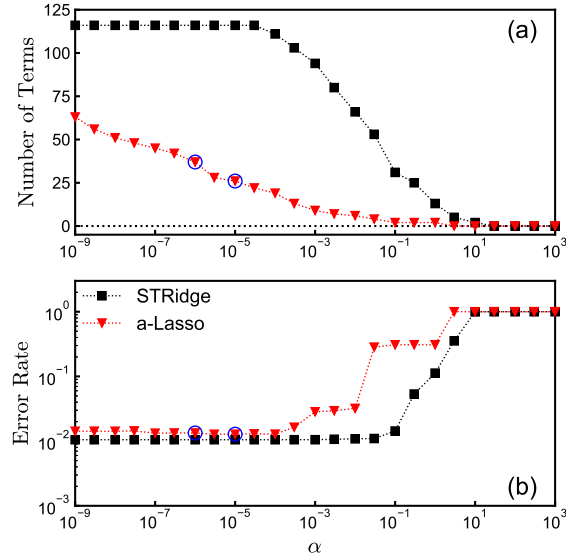


FIG. S8. (a) The total number of terms and (b) the error rate of the constitutive model obtained by *Rheo*-SINDy with the STRidge (black squares) and the a-Lasso (red reverse triangles) for the FENE dumbbell model. To obtain constitutive models, we used the training data with  $\gamma_0 = 8$ . The horizontal short-dashed line in (a) indicates that the number of terms is zero. The blue circles represent the  $\alpha$  values selected for test simulations.

$\alpha$	equations
$1 \times 10^{-6}$	$  \begin{aligned}  \dot{\tau}_{xx} = & -1.410\tau_{xx} - 9.752\tau_{yy} + 6.465\tau_{zz} + 0.095\tau_{xy} \\  & + 0.083\text{tr}\boldsymbol{\tau}\tau_{xx} + 0.259\text{tr}\boldsymbol{\tau}\tau_{yy} + 3.001\text{tr}\boldsymbol{\tau}\tau_{zz} - 0.063\text{tr}\boldsymbol{\tau}\tau_{xy} \\  & - 0.181(\text{tr}\boldsymbol{\tau})^2\tau_{yy} + 0.567(\text{tr}\boldsymbol{\tau})^2\tau_{zz} + 0.038\tau_{xx}\kappa_{xy} - 0.431\tau_{zz}\kappa_{xy} + 2.449\tau_{xy}\kappa_{xy} \\  & + 0.051\tau_{xx}\tau_{yy}\kappa_{xy} - 0.026\tau_{xx}\tau_{xy}\kappa_{xy} - 7.000\tau_{yy}^2\kappa_{xy} + 28.030\tau_{yy}\tau_{zz}\kappa_{xy} + 3.921\tau_{yy}\tau_{xy}\kappa_{xy} \\  & - 37.643\tau_{zz}^2\kappa_{xy} - 10.279\tau_{zz}\tau_{xy}\kappa_{xy} - 0.154(\text{tr}\boldsymbol{\tau})^2 \\  \dot{\tau}_{yy} = & +6.893\tau_{yy} - 14.235\tau_{zz} - 0.555\text{tr}\boldsymbol{\tau}\tau_{yy} + 1.459\text{tr}\boldsymbol{\tau}\tau_{zz} + 0.303\tau_{yy}\tau_{xy}\kappa_{xy} - 0.871\tau_{zz}\tau_{xy}\kappa_{xy} \\  \dot{\tau}_{zz} = & +2.704\tau_{yy} - 4.889\tau_{zz} \\  \dot{\tau}_{xy} = & -1.506\tau_{xy} + 1.375\kappa_{xy} - 0.078\text{tr}\boldsymbol{\tau}\tau_{xy} \\  & + 2.584\tau_{yy}\kappa_{xy} - 0.878\tau_{zz}\kappa_{xy} + 2.258\tau_{yy}^2\kappa_{xy} - 12.461\tau_{yy}\tau_{zz}\kappa_{xy} + 10.506\tau_{zz}^2\kappa_{xy}  \end{aligned}  $
$1 \times 10^{-5}$	$  \begin{aligned}  \dot{\tau}_{xx} = & -1.250\tau_{xx} - 5.341\tau_{yy} + 0.072\text{tr}\boldsymbol{\tau}\tau_{xx} + 3.823\text{tr}\boldsymbol{\tau}\tau_{zz} - 0.155(\text{tr}\boldsymbol{\tau})^2\tau_{yy} + 0.415(\text{tr}\boldsymbol{\tau})^2\tau_{zz} \\  & + 2.330\tau_{xy}\kappa_{xy} + 1.359\tau_{yy}\tau_{zz}\kappa_{xy} + 3.189\tau_{yy}\tau_{xy}\kappa_{xy} - 4.016\tau_{zz}^2\kappa_{xy} - 8.718\tau_{zz}\tau_{xy}\kappa_{xy} - 0.171(\text{tr}\boldsymbol{\tau})^2 \\  \dot{\tau}_{yy} = & +6.926\tau_{yy} - 14.256\tau_{zz} - 0.538\text{tr}\boldsymbol{\tau}\tau_{yy} + 1.418\text{tr}\boldsymbol{\tau}\tau_{zz} + 0.289\tau_{yy}\tau_{xy}\kappa_{xy} - 0.839\tau_{zz}\tau_{xy}\kappa_{xy} \\  \dot{\tau}_{zz} = & +2.704\tau_{yy} - 4.888\tau_{zz} \\  \dot{\tau}_{xy} = & -1.543\tau_{xy} + 1.395\kappa_{xy} - 0.076\text{tr}\boldsymbol{\tau}\tau_{xy} + 2.628\tau_{yy}\kappa_{xy} - 0.872\tau_{zz}\kappa_{xy} - 3.043\tau_{yy}\tau_{zz}\kappa_{xy}  \end{aligned}  $

FIG. S9. The constitutive equations of the FENE dumbbell model obtained by *Rheo*-SINDy with the a-Lasso for the training data with  $\gamma_0 = 8$ .

## REFERENCES

- <sup>S1</sup>S. L. Brunton and J. L. Proctor, and J. N. Kutz, *Proc. Nat. Acad. Sci.*, **113**, 3932 (2016).
- <sup>S2</sup>S. H. Rudy and S. L. Brunton, J. L. Proctor, and J. N. Kutz, *Sci. Adv.*, **3**, e1602614 (2017).
- <sup>S3</sup>F. Pedregosa, G. Varoquaux, A. Gramfort, V. Michel, B. Thirion, O. Grisel, M. Blondel, P. Prettenhofer, R. Weiss, V. Dubourg, J. Vanderplas, A. Passos, D. Cournapeau, M. Brucher, M. Perrot, and E. Duchesnay, *J. Mach. Learn. Res.*, **12**, 2825 (2011).
- <sup>S4</sup>H. Zou, *J. Am. Stat. Assoc.*, **101**, 1418 (2006).
- <sup>S5</sup>K. Fukami, T. Murata, K. Zhang, and K. Fukagata, *J. Fluid Mech.*, **926**, A10 (2021).
- <sup>S6</sup>R. G. Larson, *Constitutive Equations for Polymer Melts and Solutions*, Butterworths Series in Chemical Engineering (1988).
- <sup>S7</sup>H. Giesekus, *J. Non-Newtonian Fluid Mech.*, **11**, 69 (1982).
- <sup>S8</sup>Y. Mochimaru, *J. Non-Newtonian Fluid Mech.*, **12**, 135 (1983).